



## Dense molecular gas properties on 100 pc scales across the disc of NGC 3627

I Bešlić, A Barnes, F Bigiel, J Puschign, J Pety, C Herrera contreras, A Leroy, A Usero, E Schinnerer, S Meidt, et al.

### ► To cite this version:

I Bešlić, A Barnes, F Bigiel, J Puschign, J Pety, et al.. Dense molecular gas properties on 100 pc scales across the disc of NGC 3627. Monthly Notices of the Royal Astronomical Society, 2021, 506 (1), pp.963-988. 10.1093/mnras/stab1776 . hal-03473059

**HAL Id: hal-03473059**

**<https://hal.science/hal-03473059>**

Submitted on 8 Aug 2022

**HAL** is a multi-disciplinary open access archive for the deposit and dissemination of scientific research documents, whether they are published or not. The documents may come from teaching and research institutions in France or abroad, or from public or private research centers.

L'archive ouverte pluridisciplinaire **HAL**, est destinée au dépôt et à la diffusion de documents scientifiques de niveau recherche, publiés ou non, émanant des établissements d'enseignement et de recherche français ou étrangers, des laboratoires publics ou privés.

# Dense molecular gas properties on 100 pc scales across the disc of NGC 3627

I. Bešlić<sup>1</sup>,<sup>1</sup>★ A. T. Barnes<sup>1</sup>,<sup>1</sup>★ F. Bigiel<sup>1</sup>,<sup>1</sup>★ J. Puschig<sup>1</sup>,<sup>1</sup> J. Pety<sup>2,3</sup>, C. Herrera Contreras<sup>2</sup>, A. K. Leroy<sup>4</sup>, A. Usero<sup>5</sup>, E. Schinnerer<sup>6</sup>, S. E. Meidt<sup>7</sup>, E. Emsellem<sup>8,9</sup>, A. Hughes<sup>10,11</sup>, C. Faesi<sup>6,12</sup>, K. Kreckel<sup>13</sup>, F. M. C. Belfiore<sup>14</sup>, M. Chevance<sup>13</sup>, J. S. den Brok<sup>1</sup>, C. Eibensteiner<sup>1</sup>, S. C. O. Glover<sup>15</sup>, K. Grasha<sup>16,17</sup>, M. J. Jimenez-Donaire<sup>5</sup>, R. S. Klessen<sup>15,18</sup>, J. M. D. Kruijssen<sup>13</sup>, D. Liu<sup>6</sup>, I. Pessa<sup>6</sup>, M. Querejeta<sup>5</sup>, E. Rosolowsky<sup>19</sup>, T. Saito<sup>6</sup>, F. Santoro<sup>6</sup>, A. Schruba<sup>20</sup>, M. C. Sormani<sup>15</sup> and T. G. Williams<sup>15</sup>

*Affiliations are listed at the end of the paper*

Accepted 2021 June 9. Received 2021 June 7; in original form 2020 December 22

## ABSTRACT

It is still poorly constrained how the densest phase of the interstellar medium varies across galactic environment. A large observing time is required to recover significant emission from dense molecular gas at high spatial resolution, and to cover a large dynamic range of extragalactic disc environments. We present new NOEMA observations of a range of high critical density molecular tracers (HCN, HNC, HCO<sup>+</sup>) and CO isotopologues (<sup>13</sup>CO, C<sup>18</sup>O) towards the nearby (11.3 Mpc) strongly barred galaxy NGC 3627. These observations represent the current highest angular resolution (1.85 arcsec; 100 pc) map of dense gas tracers across a disc of a nearby spiral galaxy, which we use here to assess the properties of the dense molecular gas, and their variation as a function of galactocentric radius, molecular gas, and star formation. We find that the HCN(1–0)/CO(2–1) integrated intensity ratio does not correlate with the amount of recent star formation. Instead, the HCN(1–0)/CO(2–1) ratio depends on the galactic environment, with differences between the galaxy centre, bar, and bar-end regions. The dense gas in the central 600 pc appears to produce stars less efficiently despite containing a higher fraction of dense molecular gas than the bar ends where the star formation is enhanced. In assessing the dynamics of the dense gas, we find the HCN(1–0) and HCO<sup>+</sup>(1–0) emission lines showing multiple components towards regions in the bar ends that correspond to previously identified features in CO emission. These features are cospatial with peaks of H $\alpha$  emission, which highlights that the complex dynamics of this bar-end region could be linked to local enhancements in the star formation.

**Key words:** stars: formation – ISM: clouds – ISM: molecules – galaxies: evolution – galaxies: ISM – galaxies: star formation.

## 1 INTRODUCTION

Star formation occurs in the coldest, densest parts of molecular clouds. This is observed within star-forming regions in the Milky Way, where it has been shown that the star formation rate (SFR) surface density ( $\Sigma_{\text{SFR}}$ ) of individual clouds is proportional to the dense gas mass surface density (Lada & Lada 2003; Wu et al. 2005, 2010; Heiderman et al. 2010; Lada, Lombardi & Alves 2010; Lada et al. 2012; André et al. 2014; Evans, Heiderman & Vutisalchavakul 2014). However, to study individual molecular clouds in other galaxies, extragalactic surveys have historically focused on the brightest observable molecular emission lines: the low-J transitions of <sup>12</sup>CO, which for simplicity we will refer to as CO. These transitions are sensitive to the total molecular gas mass, but cannot discriminate the gas mass in the densest regime. In order to probe the latter, less abundant molecules with transitions at higher critical densities

( $n_{\text{crit}}$ ) are needed. We refer to the definition of critical density from Shirley (2015). In this work, we will also make use of the most effective critical density defined in Leroy et al. (2017b) (shortly the effective critical density, hereafter  $n_{\text{eff, crit}}$ ). The effective critical density depends on a transition, kinetic temperature, and optical depth. Molecules such as HCN, HNC, and HCO<sup>+</sup> have higher dipole moments than CO and its isotopologues and hence higher  $n_{\text{eff, crit}}$ . Therefore, emission from these molecules has been used to probe the amount of denser molecular gas, which is more closely related to star formation than the lower density molecular medium traced by low-J CO emission. The ratios between these lines and CO(1–0), in particular HCN/CO(1–0), are assumed to be a good proxy for the dense gas fraction.

In the seminal study by Gao & Solomon (2004a,b), they obtained galaxy-integrated measurements of HCN and total infrared luminosities (TIR) to determine the dense gas mass and SFR, respectively. They found a linear relation between the HCN and TIR luminosities, therefore HCN(1–0) emission appears to be directly correlated to the level of star formation activity. Gao & Solomon (2004a,b) and other studies (Gao et al. 2007; Graciá-Carpio, Graciá-Burillo &

\* E-mail: [ibeslic@uni-bonn.de](mailto:ibeslic@uni-bonn.de)(I.B.); [abarnes@uni-bonn.de](mailto:abarnes@uni-bonn.de)(A.T.B.); [bigiel@uni-bonn.de](mailto:bigiel@uni-bonn.de)(F.B.)

Planesas 2008; Krips et al. 2008; Juneau et al. 2009; García-Burillo et al. 2012; Privon et al. 2015) investigated whole galaxies and their centres. These studies were focusing on the relation on global scales, i.e. averaging over different regions with different physical characteristics. However, studies of molecular lines other than CO within extragalactic sources are difficult. The emission of these molecules (HCN,  $\text{HCO}^+$ , HNC, etc.) is typically very weak (e.g. HCN is  $\sim 20$ – $30$  times weaker than CO; Gao & Solomon 2004b), and for their detection more observing time is required.

Some other studies have investigated dense gas (HCN and  $\text{HCO}^+$ ) in giant molecular associations in nearby galaxies: in M31 (Brouillet et al. 2005), M33 (Buchbender et al. 2013), and in the outer spiral arm of M51 (Chen et al. 2017; Querejeta et al. 2019). However, in order to understand the physics in galaxy discs, we need to resolve these in regions of faint molecular emission as well.

Over the last decade, many studies have focused on observing resolved galaxy discs in faint molecular lines. Kepley et al. (2014) mapped these lines in the starburst galaxy M82 using the Green Bank Telescope (GBT). These authors found that the HCN and  $\text{HCO}^+$  emission correlates with star formation and more diffuse molecular gas. Usero et al. (2015) targeted HCN emission across 60 regions within 30 nearby galaxies at kiloparsec resolution using the Institut de Radio Astronomie Millimétrique (IRAM) 30-m telescope. This study investigated and found for the first time systematic variations in the dense gas fraction ( $f_{\text{dense}} = M_{\text{dense}}/M_{\text{mol}}$ ) traced by HCN/CO(1–0): higher values are seen in the centres of galaxies than in their outer parts. They also conclude that the star formation efficiency of dense molecular gas ( $\text{SFE}_{\text{dense}} = \text{SFR}/M_{\text{dense}}$ ) traced by the TIR/HCN luminosity ratio is lower in the centres of galaxies than in the outer disc.

The recent EMIR Multiline Probe of the ISM Regulating Galaxy Evolution (EMPIRE) IRAM 30-m EMIR survey was the first survey to obtain a sensitive wide-area mapping of so-called denser molecular gas tracers (e.g. HCN) across the discs of nine star-forming galaxies at 30 arcsec resolution ( $\sim 1$ – $2$  kpc; Bigiel et al. 2016; Jiménez-Donaire et al. 2019). Similarly, Bigiel et al. (2016) found that  $\text{SFE}_{\text{dense}}$  strongly depends on local environment in M51. Moreover, Jiménez-Donaire et al. (2019) showed that these variations are present in the full sample of nine galaxy discs. Gallagher et al. (2018a) mapped high critical density molecules (HCN,  $\text{HCO}^+$ , HNC, CS) and CO isotopologues ( $^{13}\text{CO}$ ,  $\text{C}^{18}\text{O}$ ) across four nearby galaxies at 8 arcsec or a few hundred parsec resolution using the Atacama Large Millimeter/submillimeter Array (ALMA). This study looked into the connection between the dense gas fraction, SFR, and the local environment. An important result from the above-mentioned studies was that while the fraction of denser gas increases towards the centres of galaxies, its efficiency to form stars is typically greatly reduced (Usero et al. 2015; Bigiel et al. 2016; Gallagher et al. 2018a; Jiménez-Donaire et al. 2019; Jiang et al. 2020). This result agrees well with studies in the Milky Way where it appears that the dense gas fraction and the star formation efficiency of dense gas within the Central Molecular Zone are higher and lower, respectively, compared to local Milky Way clouds (e.g. Longmore et al. 2013; Kruijssen & Longmore 2014; Barnes et al. 2017). The trend that has been seen between the TIR/HCN and HCN/CO in galactic centres, as shown in theoretical work by Kruijssen et al. (2014), and found in observations (e.g. Jones et al. 2012; Longmore et al. 2013; Usero et al. 2015), supports the idea that there is no absolute density threshold for star formation and that the overdensity relative to the background is important (e.g. Federrath & Klessen 2012). For example, going towards the centre of the galaxy, more dense gas is present, which increases the HCN/CO ratio, and, hence, it is expected to also form

stars at a higher efficiency. However, in the centre, the HCN-emitting gas is not tracing the relative overdensities, but rather the bulk dense gas, which is mostly not star forming. The use of the HCN/CO ratio as a tracer for dense, star-forming gas in these regimes is then problematic (e.g. Bigiel et al. 2016; Jiménez-Donaire et al. 2019).

Together, the studies by Usero et al. (2015), Bigiel et al. (2016), Gallagher et al. (2018a), Jiménez-Donaire et al. (2019), and Jiang et al. (2020) provide the first resolved view of dense molecular gas in galaxy discs. However, the resolution that they achieve in the extragalactic studies is still only  $\sim 500$  pc to 2 kpc. This is enough to resolve galaxy discs and distinguish central and disc regions, but it is still much bigger than the size of an individual molecular cloud (e.g.  $\sim 50$ – $100$  pc). As a result, observations like EMPIRE mix together many clouds in distinct evolutionary states (the typical distance between independent regions with distinct evolutionary states is  $\sim 100$ – $200$  pc; see e.g. Kruijssen et al. 2019; Chevance et al. 2020; Kim et al. 2021) and physical environments (Hughes et al. 2013; Colombo et al. 2014). Recent decades and years have seen rapid growth in observations of CO (Heyer & Dame 2015), which have been undertaken with single-dish telescopes (e.g. Yamaguchi et al. 1999; Dame, Hartmann & Thaddeus 2001; Moriguchi et al. 2001; Regan et al. 2001; García-Burillo et al. 2003; Helfer et al. 2003; Mizuno & Fukui 2004; Gratier et al. 2012; Burton et al. 2013; Barnes et al. 2015), as well as with the current generation of interferometer telescopes [e.g. Northern Extended Millimeter Array (NOEMA) and ALMA; e.g. Engargiola et al. 2003; Rosolowsky et al. 2003, 2021; Rosolowsky 2007; Sheth et al. 2008; Hirota et al. 2011; Schinnerer et al. 2013; Schruba et al. 2017; Egusa et al. 2018; Faesi, Lada & Forbrich 2018; Sun et al. 2018; Maeda et al. 2020; Leroy et al. 2021b]. The big step forward in terms of sensitivity, resolution, and sample size is the current Physics at High Angular-resolution in Nearby Galaxies with ALMA (PHANGS-ALMA) survey. The PHANGS-ALMA survey maps CO(2–1) emission across a sample of 74 nearby star-forming galaxies with resolution high enough to detect individual giant molecular clouds (GMCs) across galaxies’ discs (PI: E. Schinnerer; Leroy et al. 2021b; Rosolowsky et al. 2021).

The next logical step is to also map the denser gas content of individual molecular clouds. The single-dish studies have provided an insight into how the dense molecular gas is distributed in nearby galaxies (Kepley et al. 2018; Viaene, Forbrich & Fritz 2018; Watanabe et al. 2019). Moreover, despite the difficulties attaining sensitivity at high angular resolution, several works have begun to map high critical density lines down to cloud scales in nearby galaxies using interferometers (e.g. Viti et al. 2014; Murphy et al. 2015; Chen et al. 2017; Walter et al. 2017; Gallagher et al. 2018b; Querejeta et al. 2019). Observations of high critical density molecules at a high spatial resolution allow us to measure dense molecular gas as a function of cloud surface density, dynamical state, and evolutionary state. Several studies have already taken pioneering steps in this direction, mapping HCN and  $\text{HCO}^+$  emission at high physical resolution, and demonstrated the full potential of such observations despite the limited field of view, i.e. in chemical modelling (Viti et al. 2014), studying the outflows (Walter et al. 2017), investigating how the  $\text{SFE}_{\text{dense}}$  varies at 100 pc scales (Querejeta et al. 2019). Gallagher et al. (2018b) combined high-resolution CO measurements with lower resolution EMPIRE and ALMA (Atacama Compact Array – ACA) HCN maps to connect cloud properties to the dense gas fraction. However, a high resolution, sensitive, resolved HCN and  $\text{HCO}^+$  map across a large portion of a galaxy disc is still lacking within the literature.

In this work, we present new observations using the NOEMA interferometer targeting one galaxy: NGC 3627 (source information

**Table 1.** Source information.

Property	Value
Name	NGC 3627 (Messier 66)
Hubble type <sup>a</sup>	SABb
Centre RA (J2000)	11 <sup>h</sup> 20 <sup>m</sup> 14 <sup>s</sup> .867
Centre Dec. (J2000)	12°59′34″.05
Inclination, $i$ (°) <sup>a</sup>	62
Position angle, PA (°) <sup>a</sup>	173
Distance, $D$ (Mpc) <sup>b</sup>	11.3
$r_{25}$ (arcmin) <sup>b, c</sup>	5.1
$V_{\text{sys, hel}}$ (km s <sup>-1</sup> ) <sup>d</sup>	744
Metallicity ( $12 + \log(\text{O}/\text{H})$ ) <sup>e</sup>	$8.328 \pm 0.004$
$\langle \Sigma_{\text{SFR}} \rangle$ (M <sub>⊙</sub> yr <sup>-1</sup> kpc <sup>-2</sup> ) <sup>f</sup>	$7.7 \times 10^{-3}$
$\log_{10}(M_*)$ (M <sub>⊙</sub> ) <sup>g</sup>	10.5

<sup>a</sup>Morphology taken from the NASA Extragalactic Database (NED).<sup>b</sup>Distance adopted from Anand et al. (2021).<sup>c</sup>Radius of the  $B$ -band 25th mag isophote.<sup>d</sup>Systemic velocity from Casasola et al. (2011).<sup>e</sup>Metallicity calibration taken from Thuan & Izotov (2005) and metallicity value from Kreckel et al. (2019).<sup>f</sup>Average SFR surface density inside  $0.75 r_{25}$ , taken from the PHANGS-ALMA survey paper Leroy et al. (2021b).<sup>g</sup>Integrated stellar mass based on  $3.6 \mu\text{m}$  emission, taken from the PHANGS-ALMA survey paper (Leroy et al. 2021b).**Table 2.** Properties of the observed molecular lines. We tabulate the molecular transition, rest frequency, and the effective critical density (Leroy et al. 2017a) taken at a temperature of 25 K for lines studied here.

Line	$\nu_{\text{rest}}$ (GHz)	$n_{\text{eff, crit}}$ (cm <sup>-3</sup> )
<sup>12</sup> CO(2–1) <sup>a, b</sup>	230.53	$1 \times 10^3$
<sup>13</sup> CO(1–0) <sup>a, c</sup>	110.20	$8 \times 10^2$
C <sup>18</sup> O(1–0) <sup>a, c</sup>	109.78	$8 \times 10^2$
HCO <sup>+</sup> (1–0) <sup>a, d</sup>	89.19	$4 \times 10^4$
HCN(1–0) <sup>a, d</sup>	88.63	$2 \times 10^5$
HNC(1–0) <sup>a, d</sup>	90.66	$1 \times 10^5$

<sup>a</sup>Calculated from the Leiden Atomic and Molecular Database (LAMDA; Schöier et al. 2005; van der Tak et al. 2007).<sup>b</sup>The opacity of 100 adopted for this line (assuming the CO(1–0) is optically thick; Leroy et al. 2017a).<sup>c</sup>We assume a fixed optical depth of 0.1.<sup>d</sup>Here we assume a fixed optical depth of 1.

is listed in Table 1). This survey currently represents the highest resolution observations ( $1.85 \text{ arcsec} = 102 \text{ pc}$ ) across a large part of a galaxy disc using high critical density molecules (line properties are given in Table 2). We use these observations to study the physical conditions of the denser gas at the scale of individual molecular clouds, to examine how the dense molecular gas is distributed across the galaxy’s disc at these scales, and to study various density-sensitive line ratios. We investigate how dense molecular gas is linked to star formation at cloud scales. We also study various line ratios: the observed molecular lines relative to CO(2–1) and the line ratios among the high critical density molecules (HCN, HNC, and HCO<sup>+</sup>). Investigating line intensities relative to CO(2–1) emission, in particular HCN/CO(2–1), we are able to determine where the more dense molecular gas is present relative to the molecular gas content and how it is affected by the environment and star formation. Moreover, by studying the line ratios among the high critical density molecular lines such as HCN, HNC, and HCO<sup>+</sup>, we access the physical and chemical processes that set the cloud properties.

**Table 3.** NOEMA observation parameters.

Line	Beam (arcsec)	Beam (pc)	PA (°)	Noise <sup>a</sup> (mK)
HCN(1–0)	$1.87 \times 1.04$	$102.4 \times 57.0$	26	51
HCO <sup>+</sup> (1–0)	$1.86 \times 1.03$	$101.8 \times 56.4$	27	54
HNC(1–0)	$1.85 \times 1.05$	$101.2 \times 57.5$	22	54
C <sup>18</sup> O(1–0)	$1.52 \times 0.84$	$83.2 \times 46$	27	78
<sup>13</sup> CO(1–0)	$1.52 \times 0.84$	$83.2 \times 46$	27	87

<sup>a</sup>Evaluated at the mosaic phase centre, which is close to the galaxy centre (the noise steeply increases at the mosaic edges after correction for primary beam attenuation), at a spectral resolution of  $5 \text{ km s}^{-1}$ .

NGC 3627 is a nearby, star-forming galaxy with a strong bar, part of the M66 group (Leo Triplet) (Garcia 1993). It is also classified as low-ionization nuclear emission-line region (LINER)/type 2 Seyfert galaxy (Ho, Filippenko & Sargent 1997; Filho, Barthel & Ho 2000). Watanabe et al. (2019) observed three regions in NGC 3627 (the centre, a bar end, and a spiral arm) in 3-mm band using IRAM 30-m and Nobeyama 45-m telescopes. They detected  $\sim 10$  molecular species in each region, finding that the chemical composition is similar among these regions. NGC 3627 has been mapped in HCN as part of the EMPIRE survey using the IRAM 30-m telescope (Jiménez-Donaire et al. 2019) and by ALMA (Gallagher et al. 2018a). Murphy et al. (2015) found a spatial offset between the peak intensity of HCN and HCO<sup>+</sup> and tracers of recent star formation in the centre and the bar ends in NGC 3627. This study also found that the dynamical state of the gas plays a more important role in star formation than the abundance of the dense gas. Beuther et al. (2017) investigated dynamics in NGC 3627 bar ends, finding multiple velocity components in CO(2–1) that originate from orbits coming from the bar and the spiral arm.

The paper is organized as follows. In Section 2, we outline the reduction and imaging of the NOEMA observations. We summarize the ancillary observations used throughout this work in Section 2.3. In Section 3, we present the moment maps for each line, and discuss trends of the integrated intensity as a function of radius, SFR surface density, and molecular gas surface density, as well as dense gas velocity dispersion and various line ratios. In Section 4, the results of this work are discussed in the framework of our current understanding of dense molecular gas properties and star formation. Finally, in Section 5, we summarize the findings of this work.

## 2 IRAM OBSERVATIONS, ANCILLARY DATA, AND THE PRODUCTION OF INTEGRATED INTENSITY MAPS

### 2.1 IRAM observations

The observations were taken at 3 mm using both the IRAM NOEMA interferometer at Plateau de Bure and the IRAM 30-m single dish. The 3 mm continuum emission was not detected. Since a multiplicative interferometer filters out the low spatial frequencies, i.e. spatially extended emission, we used the IRAM 30-m observations to recover the low spatial frequency (‘short- and zero-spacing’) information missed by NOEMA at a depth that matches the interferometric data. In the following sections, we describe the observing strategy, calibration, joint imaging, and deconvolution processes. Table 3 summarizes the parameters of the interferometric observations.



### 2.1.1 Interferometric observations and calibration

Interferometric measurements of NGC 3627 were obtained with NOEMA. The sideband separating receivers were tuned to observe from 86.9 to 94.6 GHz (lower sideband) and from 102.4 to 110.1 GHz (upper sideband). The POLYFIX correlator yielded a total bandwidth of  $2 \times 7.7$  GHz per polarization at a spectral channel spacing of 2 MHz. Each intermediate-frequency baseband was further split into up to  $16 \times 64$  MHz chunks of high spectral channel spacing. These chunks were centred around potential lines inside the lower and upper sidebands. This yielded spectra with a 62.5 kHz channel spacing that we further smoothed to reach three different spectral resolutions: 5, 10, and 20  $\text{km s}^{-1}$ . In short, the frequency set-up was chosen to simultaneously cover the  $J = 1-0$  lines of  $^{13}\text{CO}$  and  $\text{C}^{18}\text{O}$  in the upper sideband, and the  $J = 1-0$  lines of  $\text{HCO}^+$ , HCN, and HNC in the lower sideband. Their frequencies are listed in Table 2.

We observed a mosaic of six pointings aligned along the bar of NGC 3627 at a position angle (PA) of  $-26^\circ$ . The neighbouring pointings were separated by 22.5 arcsec, which is half the primary beam size at 110 GHz. The mosaic thus covers a roughly rectangular field of view of about  $2.7 \times 0.9$  arcmin<sup>2</sup> ( $\approx 1.5 \times 0.5$  kpc<sup>2</sup>). These measurements were carried out with eight or nine antennas in the C and A configurations (baselines from 15 to 750 m) from 2018 February to May. This amounts to 30.5 h of telescope time (12 h in C and 18.5 h in A configurations). The on-source time is equal to 8.8 h with a nine-antenna array. During the observations, the typical precipitable water vapour ranged from 1 to 3 mm in A configuration and 3 to 8 mm in C configuration. The typical system temperature was between 70 and 150 K, depending on the weather.

We used the standard algorithms implemented in the GILDAS/CLIC software to calibrate the NOEMA data.<sup>1</sup> The radio-frequency bandpass was calibrated by observing the bright quasars 3C 84 ( $\sim 14$  Jy), 3C 279 ( $\sim 15$  Jy), and 0851+202 ( $\sim 5$  Jy). Phase and amplitude temporal variations were calibrated by fitting spline polynomials through regular measurements of two nearby quasars (1222+216 with a flux of about 2.0 Jy at 17.5 distance, and 1116+128 with a flux of about 0.5 Jy at 0.5 distance). One of the NOEMA secondary flux calibrators (either MWC 349 or LKH $\alpha$  101) was observed during each track, which allowed us to improve the accuracy of the absolute flux scale of the interferometric data to  $\sim 10$  per cent.

### 2.1.2 Joint imaging and deconvolution of the interferometric and single-dish data

The single-dish observations were taken with the IRAM 30-m telescope as part of the EMPIRE large program (PI: F. Bigiel) from 2014 December to 2016 December. Jiménez-Donaire et al. (2019) describe in detail the observations and data reduction.

Following Rodríguez-Fernández, Pety & Gueth (2008), the GILDAS/MAPPING software and the single-dish data from the IRAM 30-m were used to create the short-spacing visibilities not sampled by NOEMA using the UV\_SHORT task. In short, the 30-m data cubes were first resampled around the redshifted frequencies observed with NOEMA and reprojected to the NOEMA phase centre. The data cubes were deconvolved from the IRAM 30-m beam in the Fourier plane, and corrected for the NOEMA primary beam response in the image plane. After a last Fourier transform, pseudo-visibilities were

sampled between 0 and 15 m, the difference between the diameters of the IRAM 30-m and the 15-m NOEMA antennas. These visibilities were then merged with the interferometric observations.

Each mosaic field was imaged and a dirty mosaic was built combining those fields in the following optimal way in terms of signal-to-noise ratio (S/N; Pety & Rodríguez-Fernández 2010). The dirty cube is corrected for primary beam attenuation, which induces a spatially inhomogeneous noise level. In particular, noise strongly increases near the edges of the field of view. To limit this effect, both the primary beams and the resulting dirty mosaics are truncated. The standard level of truncation is set at 20 per cent of the maximum in GILDAS/MAPPING. The dirty image is deconvolved using the standard Högbom CLEAN algorithm. CLEAN components were only searched for inside a mask produced from the EMPIRE  $^{12}\text{CO}(1-0)$  cube obtained at the IRAM 30-m telescope. Pixels within each channel with an S/N of the  $\text{CO}(1-0)$  line larger than 3 are included in this three-dimensional mask. This gives a shallow mask that loosely follows the galaxy velocity pattern as the angular resolution is 27 arcsec and the typical sensitivity is good ( $\sim 10$  mK). The resulting data cubes are then scaled from Jy beam<sup>-1</sup> to main beam brightness temperature ( $T_b$ ) scale using the synthesized beam size (see Table 3). The channel width of the final data cubes is 5  $\text{km s}^{-1}$ . The resulting beam size and corresponding noise values of the final combined maps used throughout this work are presented in Table 3.

## 2.2 The production of integrated intensity maps

We produce integrated intensity maps from masked spectral cubes for each line. The mask is based on the ALMA  $\text{CO}(2-1)$  cube (resolution 1.5 arcsec), because we expect to detect HCN emission only in regions of the galaxy with detected CO emission (Jiménez-Donaire et al. 2019; Querejeta et al. 2019). We convolve all NOEMA data cubes to a common working resolution of  $1.95 \times 1.95$  arcsec<sup>2</sup>  $\times$  5  $\text{km s}^{-1}$  ( $1.95$  arcsec  $\approx 102$  pc). The ALMA  $\text{CO}(2-1)$  cube (see the following section for more details) has been spectrally and spatially smoothed and regridded to match the NOEMA observations.

We make use of an expanding masking technique in order to create masks for our data set (Pety et al. 2013). To construct the mask, we calculate the three-dimensional noise cube from signal-free parts of the spectrum. Then we define an initial mask where we select all pixels with S/N higher than 4 over at least two neighbouring channels. The mask is then expanded to cover all the pixels defined by a lower 2 S/N mask (Rosolowsky & Leroy 2006).

We apply the  $\text{CO}(2-1)$  mask to all of our line data cubes, and we determine the integrated intensity maps by summing intensities along the velocity axis for all lines of sight and multiplying by the channel width ( $\Delta v = 5$   $\text{km s}^{-1}$ ). We construct a two-dimensional noise map ( $\Delta_{\text{rms}}$ ) based on the signal-free parts of each spectrum. Then we estimate the uncertainty in the integrated intensity by scaling this value by the channel width  $\Delta v$  and the square root of the number of signal channels  $N$ :

$$\Delta_I = \Delta_{\text{rms}} \Delta v \sqrt{N}. \quad (1)$$

The S/N is then calculated by dividing the integrated intensity map by this uncertainty map.

## 2.3 Ancillary data

Throughout this work, we make use of a set of ancillary observations to determine the molecular gas and SFR surface densities. These are summarized in this section.

<sup>1</sup>See <http://www.iram.fr/IRAMFR/GILDAS> for more information on the GILDAS software (Pety 2005).

### 2.3.1 PHANGS-ALMA CO(2–1)

As a tracer of the molecular gas surface density in NGC 3627, we make use of CO(2–1) molecular line observations obtained with the ALMA interferometer. These were performed as part of the PHANGS-ALMA survey (PI: E. Schinnerer; Leroy et al. 2021b). Both 12-m array, 7-m array and the total power antennae (ACA) were used for the mosaic observations, therefore full spatial information is recovered for the whole CO disc of NGC 3627. The interferometric data were calibrated with the ALMA calibration pipelines and imaged with the PHANGS-ALMA pipeline (Leroy et al. 2021a). The total power data were calibrated following the method presented by Herrera et al. (2020). Then, interferometric and total power data were aligned, combined with the CASA feather task, and post-processed to  $T_b$  cubes using the PHANGS-ALMA pipeline. Moment maps were also generated with this pipeline. The data we used in this work are from the internal data release version 3.4 processed with the PHANGS-ALMA pipeline version 1. We refer the reader to Leroy et al. (2021b) for more details about the data processing. Imaging was done using CASA version 5.4.0. After calibration and imaging, the data cube was convolved to produce a round beam. The typical rms noise in brightness temperature units is  $\sim 0.17$  K per  $2.5 \text{ km s}^{-1}$  channel (see also Schinnerer et al. 2019). In our work, we use a CO(2–1) data cube convolved to  $1.95 \text{ arcsec}$  resolution with the channel width of  $5 \text{ km s}^{-1}$ .

### 2.3.2 PHANGS-MUSE H $\alpha$ data

We determine the SFR in NGC 3627 from the  $1.5 \text{ arcsec}$  H $\alpha$  map observed with the Multi-Unit Spectroscopic Explorer (MUSE)/Very Large Telescope (VLT). These observations were performed as part of the PHANGS-MUSE survey. We make use of data from internal release version 2.0 (PI: E. Schinnerer; see Emsellem et al., in preparation, for full details of data reduction). To estimate the SFR at each pixel, we make use of the MUSE extinction-corrected H $\alpha$  map at  $1.95 \text{ arcsec}$  resolution. The extinction is calculated using the measured Balmer decrement assuming case B recombination, i.e. an intrinsic H $\alpha$ /H $\beta$  ratio of 2.86, which corresponds to a temperature of  $10^4 \text{ K}$  and electron density of  $100 \text{ cm}^{-3}$  (Osterbrock 1993; Domínguez et al. 2013). The recombination coefficients are robust to realistic changes in temperature and density (Osterbrock 1989). We make use of a Calzetti et al. (2000) extinction curve, and for the extinction-corrected map, only H $\alpha$  and H $\beta$  with an S/N better than 15 are used, whereas the values below this threshold are masked (see Faesi et al., in preparation, for full details on the extinction correction).

In addition to being produced in the nebulae ionized by massive young stars, H $\alpha$  photons can originate from a wide range of other ionizing sources: gas ionized by an active galactic nucleus (AGN), older stellar populations, planetary nebulae (PNe), and supernovae. Thus simply adding up all H $\alpha$  emission could overestimate the SFR and therefore bias our results. In order to ensure that we only make use of the H $\alpha$  emission associated with star formation, we first match the H II region catalogue of Santoro et al. (in preparation), which uses two algorithms for finding spatially resolved (HIIPHOT; Thilker, Braun & Walterbos 2000) and point-like H II regions (DAOSTARFINDER; Stetson 1987) to isolate H $\alpha$  emission associated with massive star formation. Then we mask our H $\alpha$  map. However, this is not enough, since H $\alpha$  photons within H II regions can still in principle originate from sources other than star formation. We further apply a Baldwin–Phillips–Terlevich (BPT; Baldwin, Phillips & Terlevich 1981) cut with line luminosity (in units of solar luminosity –  $L_\odot$ ) ratio

thresholds of  $\log[\text{N II}]/\text{H}\alpha < 0$  and  $\log[\text{O II}]/\text{H}\beta < -0.09$  (Baldwin et al. 1981; Kewley et al. 2001; Kauffmann et al. 2003). With these criteria, we remove all the pixels within the H II regions coming from ionizing sources other than the star-forming ones. All sightlines that do not satisfy these criteria are treated as a not a number (NaN). The H II mask and the BPT cut remove  $\sim 40$  per cent of the total H $\alpha$  flux from the initial H $\alpha$  map.

This map is then converted to the SFR surface density,  $\Sigma_{\text{SFR}}$ , following Calzetti et al. (2007),

$$\Sigma_{\text{SFR}} = \frac{10^{-41.27} (3.08 \times 10^{21})^2 S_{\text{H}\alpha} 4\pi}{\Omega}, \quad (2)$$

where  $\Omega$  is the pixel angular area in steradian (sr),  $S_{\text{H}\alpha}$  is the H $\alpha$  flux per pixel in units of  $\text{erg s}^{-1} \text{ cm}^{-2}$ , and  $(3.08 \times 10^{21})^2$  is the  $\text{kpc}^2$  to  $\text{cm}^2$  scaling factor. The factor of  $5.37 \times 10^{-42}$  has been calculated with assumptions that the H $\alpha$  has already been corrected for dust extinction, and a fully populated Kroupa initial mass function (IMF; Kroupa 2001) taken over the range of stellar masses  $0.1$ – $100 M_\odot$  (Murphy et al. 2011; Kennicutt & Evans 2012). The use of H $\alpha$  emission provides an almost instantaneous measure of the SFR, tracing activity over the past  $\sim 10$ – $100 \text{ Myr}$  (see Kennicutt & Evans 2012).

We note here several issues related to the conversions of H $\alpha$  emission to SFR, which are particularly relevant when assessing the SFR over small spatial scales (e.g.  $100 \text{ pc}$  scales). First, the high sampling rate at high resolution, can return regions with a low SFR ( $\Sigma_{\text{SFR}} < 10^{-3} M_\odot \text{ yr}^{-1} \text{ kpc}^{-2}$ ), within which the IMF can become poorly sampled. The conversion from H $\alpha$  emission that assumes a fully sampled IMF may then under- or overestimate the SFR (e.g. Lee et al. 2009; Querejeta et al. 2019). The IMF can be poorly sampled on smaller spatial scales where we probe either lower mass clusters or lower SFRs, which can cause some stochastic variation in the calculated SFR (Kennicutt & Evans 2012). Secondly, the H $\alpha$  line is subject to systematic uncertainties from dust attenuation and excitation variations in galaxies. Thirdly, the H $\alpha$  emission relies on the production of ultraviolet (UV) photons from massive ( $> 10 M_\odot$ ) stars, which ionize the surrounding medium. Regions containing exclusively lower mass stars or which are well mixed with the diffuse ionized gas are, therefore, not seen in H $\alpha$  emission, and not accounted for in our measurement of the SFR.

To estimate how much star formation is not traced by our extinction-corrected H $\alpha$  emission due to extinction, we compare to SFR estimates from a combination of far-ultraviolet (FUV) emission and mid-infrared (mid-IR) emission. For that purpose, we use the  $\Sigma_{\text{SFR}}$  map from Leroy et al. (2019). We use the  $\Sigma_{\text{SFR}}$  map determined from FUV +  $22 \mu\text{m}$  and convert to SFR by multiplying each value by the projected pixel surface area ( $0.075 \text{ kpc}^2$  for a  $5 \times 5 \text{ arcsec}^2$  pixel). We compare values coming within the radius of  $\sim 1 \text{ kpc}$  from the centre of NGC 3627, and from the rest of the mapped region. For the central region, we measure a SFR of  $\sim 0.016 M_\odot \text{ yr}^{-1}$  from the extinction-corrected H $\alpha$  emission and  $\sim 0.286 M_\odot \text{ yr}^{-1}$  from FUV +  $22 \mu\text{m}$ . For the rest of the NGC 3627, the SFR traced by the extinction-corrected H $\alpha$  is  $\sim 1.27 M_\odot \text{ yr}^{-1}$ , whereas the SFR traced by FUV +  $22 \mu\text{m}$  is  $\sim 1.55 M_\odot \text{ yr}^{-1}$ . The large difference in SFR from the centre of NGC 3627 is due to the fact that H $\alpha$  emission associated with the AGN has been removed in the map used here, where it remains within the FUV +  $22 \mu\text{m}$  SFR estimate. Whereas, in the rest of the galaxy, where both the FUV +  $22 \mu\text{m}$  and H $\alpha$  emission are expected to better trace the star formation, we estimate that they are in agreement (i.e. within 17 per cent). The small difference could be due to the high obscuration of the H $\alpha$  emission from deeply embedded star-forming regions, not corrected for by the

Balmer decrement extinction correction, which then otherwise emit at longer wavelengths (i.e. as seen at 24  $\mu\text{m}$ ; e.g. see Kennicutt et al. 2009; Kim et al. 2021).

### 3 RESULTS

#### 3.1 Integrated intensity maps

Fig. 1 shows the ancillary data (first row) towards NGC 3627 (Section 2.3) and the integrated intensity maps (second row) for HCN,  $^{13}\text{CO}$ , and  $\text{HCO}^+$ . We show the remainder of the detected lines, HNC and  $\text{C}^{18}\text{O}$ , in the bottom row of Fig. 1. The overlaid contours in the top row show the  $3\sigma$ ,  $5\sigma$ , and  $10\sigma$  S/N of HCN emission. The median uncertainty of the HCN integrated intensity across the mapped region is  $2 \text{ K km s}^{-1}$ . The corresponding  $3\sigma$  sensitivity threshold for HCN is then  $6 \text{ K km s}^{-1}$ , which, assuming a  $\text{CO}(1-0)/\text{HCN}$  ratio of 30 (Gao & Solomon 2004b) and a  $\text{CO}(1-0)$ -to- $\text{H}_2$  conversion factor of  $1.2 \text{ M}_\odot (\text{K km s}^{-1} \text{ pc}^{-2})^{-1}$  calculated for NGC 3627 (Bolatto, Wolfire & Leroy 2013; Sandstrom et al. 2013), implies a mass sensitivity of  $\sim 216 \text{ M}_\odot \text{ pc}^{-2}$ .

In Fig. 2, we show the fraction of the total observed area that has significant detections from each of the observed molecular lines as a function of their effective critical density listed in Table 2. This area includes positions within the mosaic that have an integrated intensity value higher than three times the associated uncertainty (ranges for one and ten times the uncertainty are shown as error bars). In general, we find that the emission of high critical density lines is much more spatially compact than the  $\text{CO}(2-1)$  emission. The isotopologues of CO have a similar effective critical density, yet exhibit comparable coverage to the higher critical density lines. This can naturally be explained by the lower abundances of the CO isotopologues relative to  $^{12}\text{CO}$ , which causes weaker line emission that falls below our detection limit. Of the observed lines, we see that the  $^{13}\text{CO}$  line is the brightest and most spatially extended, whereas  $\text{C}^{18}\text{O}$  is the faintest and most compact (see Fig. 1).

#### 3.2 Stacking procedure

In order to recover emission from the low signal/noise lines of sight, we stack individual spectra as a function of galactocentric radius, SFR surface density, and  $\text{CO}(2-1)$  integrated intensity following Schrubba et al. (2011), Caldú-Primo & Schrubba (2016), and Jiménez-Donaire et al. (2017, 2019). To do this, first we convolve our data cubes and maps to a common angular and spectral resolution of 1.95 arcsec and  $5 \text{ km s}^{-1}$ , respectively. Next, we regrid all data cubes and maps to a common world coordinate system (WCS). Last, we resample our line emission maps (including the ancillary data) on to the same hexagonal grid, where sampling points are spaced by half a beam size of the NOEMA observations ( $\sim 1 \text{ arcsec}$ ), thus oversampling the data by a factor of 4.

Then we measure the average integrated intensity of each observed line in each bin. To do this, first we calculate the velocity at which the  $\text{CO}(2-1)$  spectrum peaks within all the lines of sight. In the next step, we shift the spectra of each line of sight within the NOEMA and ALMA  $\text{CO}(2-1)$  cubes by the velocity previously defined. This procedure results in cubes where all molecular line emission peaks at a velocity close to  $0 \text{ km s}^{-1}$ . Averaging the shifted lines will increase the S/N and by construction one knows where a (potentially weak) spectral line should build-up. It should be highlighted, however, that this method relies on the robust detection of at least one bright line to determine the line-of-sight velocity by which all other spectra will be shifted. Typically,  $\text{CO}(2-1)$  is the brightest line along each line of

sight, so this is used as a prior. We exclude sightlines where  $\text{CO}(2-1)$  is not robustly detected, since we are unlikely to detect the weaker line emission towards these positions.

We integrate the stacked spectrum to determine the average integrated intensity of the line. We use stacked  $\text{CO}(2-1)$  spectra as a prior to determine the width of the integration window. First, we define the signal-free part of the spectrum. Next, we determine where the spectral line is defined using the masking technique described in Section 2.2. We select all channels with S/N above 4 and expand the mask to cover all neighbouring channels with S/N above 2. Finally, this velocity window is used as a mask that we apply to the stacked spectra of the rest of the observed molecular lines. The integrated intensity is then calculated as a sum over the integration window multiplied by the channel width. The uncertainty of the integrated intensity is computed using the equation (1). Because we estimate the noise from the signal-free region of the stacked spectrum itself, this uncertainty properly accounts for any spatial oversampling, as well as for the potential spatial and spectral correlation of the data. This implies that the uncertainty of the integrated intensity varies across different sightlines and from tracer to tracer. We take the integrated intensity of the stacked spectrum if the following criteria are not satisfied. In cases when  $\text{CO}(2-1)$  is detected, we measure the integrated intensity of the stacked spectrum, its peak, and the values in the two channels next to the peak. We then determine their S/N. If either of the S/Ns are below 3, the integrated intensity is taken as an upper limit of three times the uncertainty of the integrated intensity defined in equation (1). In cases where  $\text{CO}(2-1)$  is not detected (S/N < 3) and therefore the velocity window cannot be determined, we calculate the integrated intensity as an upper limit of three times the uncertainty of the integrated intensity that is calculated as the rms noise of the line multiplied by a  $30 \text{ km s}^{-1}$  velocity window. The stacked spectra and integration windows are shown in Figs A1–A3 in Appendix A.

#### 3.3 Stacking results

We stack the observed lines by the quantities measured at high spatial resolution: galactocentric radius,  $\text{CO}(2-1)$  integrated intensity, and SFR surface density. These stacked line profiles are shown in the top left-hand panels in Figs 3–5.

We define radial bins in linear space, using a radial bin size of 350 pc, which is approximately three times the beam size along the beam major axis. For stacking by  $\text{CO}(2-1)$  integrated intensity, we use data points with an S/N in  $\text{CO}(2-1)$  integrated intensity greater than 12 due to lack of the emission of dense molecular tracers at fainter sightlines. This threshold selects 70 per cent of data points that contain bright  $\text{CO}(2-1)$  emission. To stack by  $\text{CO}(2-1)$  and  $\Sigma_{\text{SFR}}$ , we define bins with widths of  $10^{0.2} (\text{K km s}^{-1})$  and  $10^{0.25} (\text{M}_\odot \text{ yr}^{-1} \text{ kpc}^{-2})$ , respectively, in logarithmic space. To illustrate which parts of the galaxy entered which specific bin, we colour code data points that contribute to the same bin and show them in the bottom right-hand panels of Figs 3–5. The  $\text{CO}(2-1)$  bins are constructed in a way that the two brightest  $\text{CO}(2-1)$  bins contain the very central part of NGC 3627, the following bins contain sightlines from the bar ends, and finally, the remaining bins contain fainter  $\text{CO}(2-1)$  sightlines located along the spiral arms and the outskirts of the central region, bar, and the bar ends. The mid-high  $\text{CO}(2-1)$  bins are associated with a few largest  $\Sigma_{\text{SFR}}$  bins.

The galactocentric radius stacks are shown in the top left-hand panel of Fig. 3. In this figure, we label where different environments are located. Overall, all lines show the strongest emission in the centre of NGC 3627, after which their emission steadily decreases



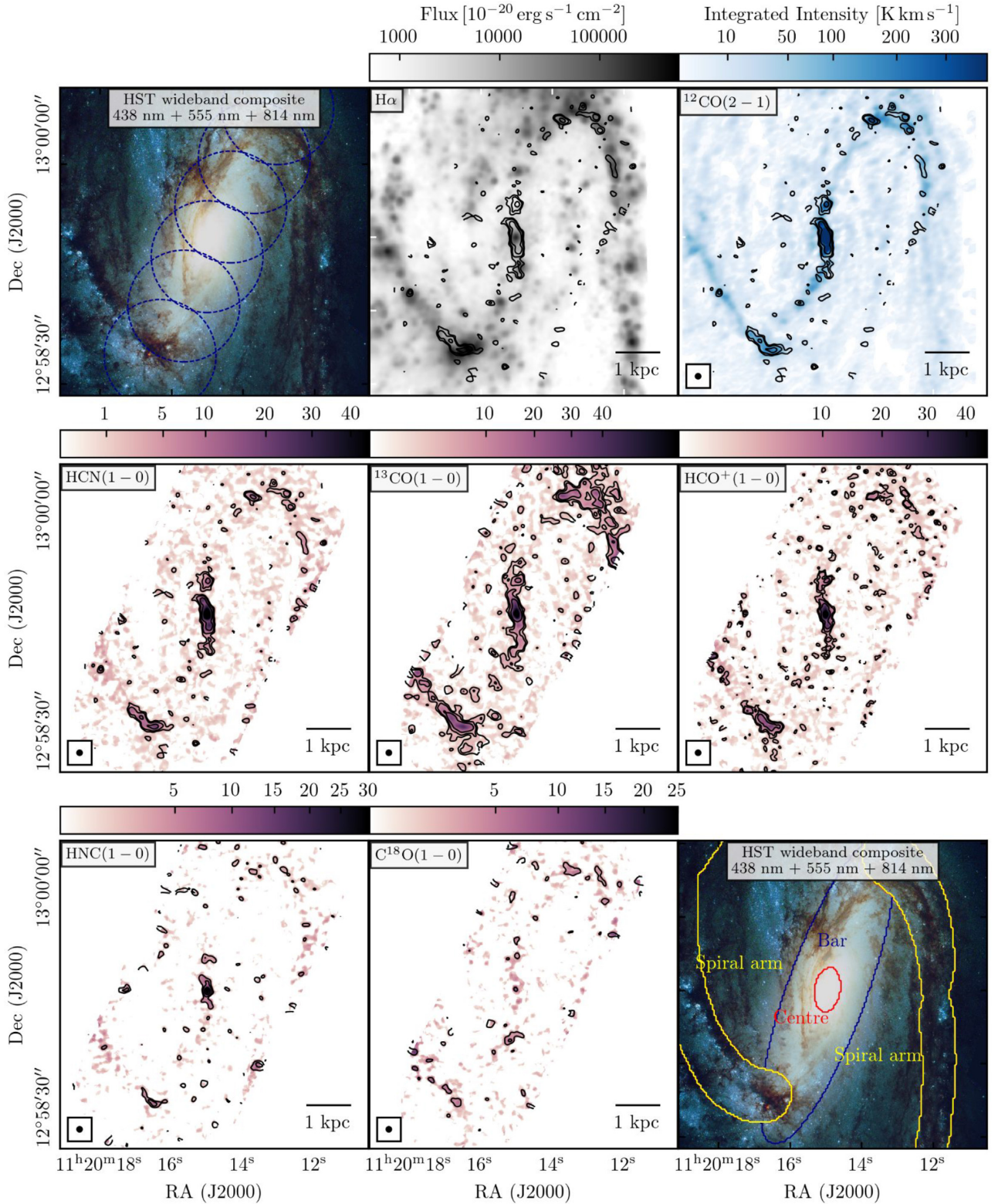


**Figure 1.** Top row: pointing pattern of the NOEMA mosaic corresponding to a frequency of 109.93 GHz overlaid on the wide field composite image of NGC 3627 obtained with the *Hubble Space Telescope* (left-hand panel; Lee et al. 2021), extinction-corrected  $H\alpha$  map at 1.86 arcsec ( $\approx 100$  pc) resolution taken by the PHANGS-MUSE survey – we show all the  $H\alpha$  emission here, i.e. BPT and H II masking is applied to this image in a later step to recover actual SFR (middle panel, see Section 2.3; Emsellem et al., in preparation), CO(2–1) integrated intensity map at 1.95 arcsec ( $\approx 107$  pc) taken by the PHANGS-ALMA survey (right-hand panel; Leroy et al. 2021b). Contours show HCN(1–0) integrated intensity at  $3\sigma$ ,  $5\sigma$ , and  $10\sigma$  levels (see below). Middle row: HCN,  $^{13}\text{CO}$ , and  $\text{HCO}^+$  integrated intensity map in  $\text{K km s}^{-1}$  observed by NOEMA at the working resolution of 1.95 arcsec ( $\approx 107$  pc) adopted in this work. Bottom row: same as in the middle row but for HNC and  $\text{C}^{18}\text{O}$ . Contours in the middle and bottom row show levels of 3, 5, and 10 of S/N for each line. The circle on the bottom left-hand corner of the integrated intensity maps is the synthesized beam (1.95 arcsec). Bottom right-hand panel: same as in the top left-hand panel with overlaid contours of environmental masks (Querejeta, in preparation).



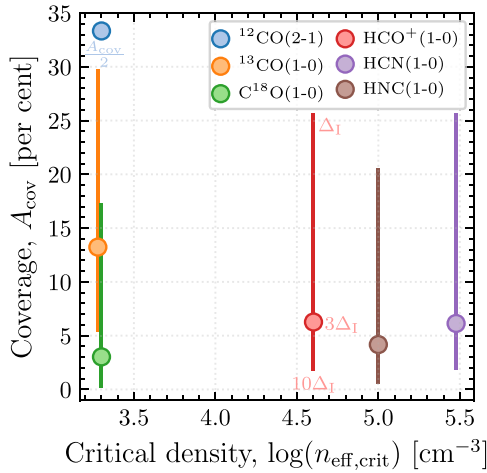


**Figure 2.** The percentage of pixels within the observed area that have significant values of the integrated intensity for each of the molecular lines,  $A_{\text{cov}}$ . We define significant integrated intensity values as being higher than three times their associated uncertainty ( $\Delta_I$ ; see Section 2.2). The error bars show the range of the percentage coverage for one and ten times the associated uncertainty. The variation between these limits for CO(2–1) line is small, therefore the error bar is not visible on the plot. The molecular line transitions are ordered as a function of the effective critical density of emission. We note that we offset the position of the  $^{13}\text{CO}$  and  $\text{C}^{18}\text{O}$  values on the x-axis to avoid overlapping, due to their similar effective critical density (Table 2). We also note that the coverage of the  $^{12}\text{CO}$  emission has to be reduced by a factor of 2 for plotting.

towards the bar where it reaches its minimum around 2 kpc (except for  $\text{C}^{18}\text{O}$  and HNC, where we do not recover emission). Line integrated intensities then increase towards the bar ends. The emission from the  $^{13}\text{CO}$  line is recovered in almost all bins, up to  $\sim 5$  kpc. The  $^{13}\text{CO}$  intensity increases towards the centre and the bar ends, but the centre appears to be brighter than the bar ends. Cormier et al. (2018) reported the opposite (i.e. brighter  $^{13}\text{CO}$  in the bar ends than in the centre), but it was noted that this might be due to the low resolution at which the line was observed ( $\sim 1.5$  kpc, compared to  $\sim 100$  pc in this work). Fig. 3 shows that the bright  $^{13}\text{CO}$  at the bar ends covers a larger radial range than the emission at the centre.

HCN and  $\text{HCO}^+$  emission are recovered along the bar ( $\sim 2$  kpc). We find that HCN and  $\text{HCO}^+$  have similar integrated intensities in the centre (26 and 21  $\text{K km s}^{-1}$ , respectively) and across the disc of NGC 3627. This was also shown for the inner  $\sim 4$  kpc region in NGC 3627 by Gallagher et al. (2018b) and Jiménez-Donaire et al. (2019). Furthermore, we see bright and constant HCN and  $\text{HCO}^+$  emission across the bar ends ( $\sim 3$ – $4$  kpc), where  $\text{HCO}^+$  is slightly brighter than HCN. Similar emission is seen in HNC, but HNC is overall fainter than HCN by a factor of 2–3.  $\text{C}^{18}\text{O}$  is the faintest in the centre in comparison with other lines from our sample. Jiménez-Donaire et al. (2019) reported similar results for HNC and  $\text{C}^{18}\text{O}$  in this galaxy. We do not see a clear trend for  $\text{C}^{18}\text{O}$  and HNC, given their emission is only significant in the bar end and in the centre and bar end, respectively (see discussion in Section 4).

In the top left-hand panel of Fig. 4, we show the line integrated intensities as a function of CO(2–1) emission. The integrated intensity of all lines increases with increasing CO(2–1) integrated intensity. Taken at face value, this result implies that when more molecular gas is present, there is also more dense molecular gas. The brightest lines in our data set,  $^{13}\text{CO}(1-0)$ , HCN, and  $\text{HCO}^+$ , are recovered in all bins. We find that HCN and  $\text{HCO}^+$  emission is considerably weaker in the

lower CO(2–1) bins in comparison with  $^{13}\text{CO}$ . Across all the CO(2–1) bins, HCN and  $\text{HCO}^+$  show similar integrated intensities.  $\text{HCO}^+$  emission is brighter than HCN for CO(2–1) integrated intensities less than  $200 \text{ K km s}^{-1}$ , whereas for the higher CO(2–1) values we find the opposite. At the very brightest CO(2–1) bin, HCN shows the brightest emission ( $\sim 110 \text{ K km s}^{-1}$ ), followed by  $^{13}\text{CO}$  and  $\text{HCO}^+$  (103 and  $76 \text{ K km s}^{-1}$ , respectively). HNC emission is recovered in almost all the CO(2–1) bins but is weaker than HCN and  $\text{HCO}^+$ . Finally, we recovered the emission of the faintest line in our data set,  $\text{C}^{18}\text{O}$ , in half of the CO(2–1) bins.

In the top left-hand panel of Fig. 5 we show line integrated intensities as stacked by SFR surface density. The emission of the stacked lines is recovered for about half of the  $\Sigma_{\text{SFR}}$  bins. We note that the central region (where the observed molecular lines peak) is excluded for analysis in this case due to the  $\text{H}\alpha$  emission not being sensitive to the presence of an embedded star formation present in this region (see Section 2.3). We find that at  $\Sigma_{\text{SFR}}$  values of  $10^{-1}$ – $1 \text{ M}_{\odot} \text{ yr}^{-1} \text{ kpc}^{-2}$  all the line intensities of denser molecular gas tracers are approximately flat, i.e. vary by a factor of  $\leq 2$ . This behaviour is different from the one seen when stacking by CO(2–1) integrated intensity (Fig. 4). Overall, line intensities show a higher correlation with CO(2–1) than with  $\Sigma_{\text{SFR}}$ . In the bottom right-hand panel of Fig. 5, where we show a map of the SFR surface density plotted over the HCN integrated intensity map, we see that HCN emission is also present in regions where there is no star formation traced by  $\text{H}\alpha$  emission. 24 per cent of the total HCN (and 27 per cent of the CO(2–1)) flux is present in regions with star formation traced by  $\text{H}\alpha$  emission.

$^{13}\text{CO}$  has overall the highest integrated intensity compared to the other observed 3 mm lines. For  $\Sigma_{\text{SFR}}$  of  $5.3 \text{ M}_{\odot} \text{ yr}^{-1} \text{ kpc}^{-2}$ ,  $^{13}\text{CO}$  has an integrated intensity of  $22 \text{ K km s}^{-1}$ . The HCN and  $\text{HCO}^+$  integrated intensities are a factor of  $\sim 2$  lower than the  $^{13}\text{CO}$  (both  $\sim 11 \text{ K km s}^{-1}$ ). Fig. 5 shows that the HCN integrated intensity is approximately constant over 1 dex in  $\Sigma_{\text{SFR}}$ , whereas for  $\Sigma_{\text{SFR}}$  greater than  $1 \text{ M}_{\odot} \text{ yr}^{-1} \text{ kpc}^{-2}$ , HCN intensity increases by  $\sim 0.6$  dex. HNC emission appears to decrease from 0.2 to  $1 \text{ M}_{\odot} \text{ yr}^{-1} \text{ kpc}^{-2}$ , but its emission increases at  $1 \text{ M}_{\odot} \text{ yr}^{-1} \text{ kpc}^{-2}$  as the rest of the lines. The increasing trend of dense gas tracers with higher values of  $\Sigma_{\text{SFR}}$  we found is in agreement with Gallagher et al. (2018a) who showed that the denser gas mass traced by HCN correlates with SFR (in their work traced by  $\text{H}\alpha$  and  $24 \mu\text{m}$  emission) in NGC 3627. Here we report similar results for the  $\text{C}^{18}\text{O}$  line as we have done in previous paragraphs.  $\text{C}^{18}\text{O}$  is the faintest line shown in Fig. 5, with emission only recovered in three  $\Sigma_{\text{SFR}}$  bins.

### 3.4 Comparison of the CO and HCN velocity dispersion

At low spatial resolution ( $\gg 100$  pc), relative motions of the molecular gas caused by the galactic potential are thought to be the dominant factor broadening molecular line profiles. Hence, it is not possible to measure the intrinsic velocity dispersion of cold, denser clumps caused by their internal dynamics (e.g. turbulence and thermal motions). However, at scales of  $\sim 100$  pc, we probe smaller clumps. GMCs are also thought to decouple from the galactic dynamical environment at these spatial scales (e.g. Meidt et al. 2018; Chevance et al. 2020), and, hence, with high spatial resolution observations we might be able to measure these intrinsic properties.

Here we present the velocity dispersion of the HCN line emission, which we compare to the velocity dispersion of CO(2–1) emission. We conduct the following method to measure the velocity dispersions of these molecular lines. The velocity dispersion calculation is based

## Radial stacks

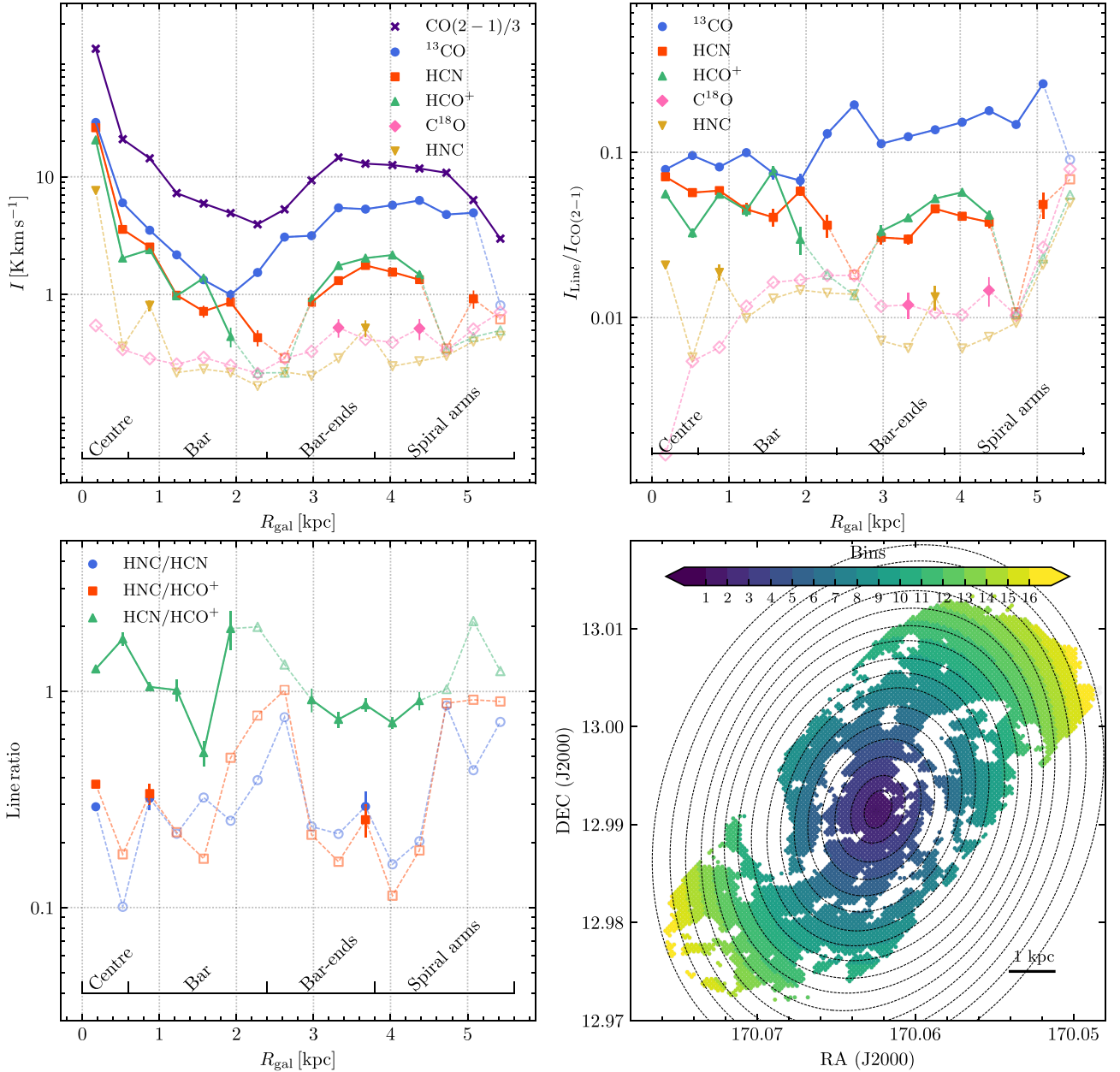


**Figure 3.** Stacked molecular line intensities binned by galactocentric radius. We show the integrated intensities of CO(2–1), CO isotopologues ( $^{13}\text{CO}$  and  $\text{C}^{18}\text{O}$ ), and the dense gas tracers in the top left-hand panel and the line ratios of dense gas tracer per unit CO(2–1) in the top right-hand panel. Line ratios among the dense gas tracers are shown in the bottom left-hand panel. All significant measurements (characterized as good and satisfactory detections) are connected with solid lines, whereas for non-detections we plot  $3\Delta_I$  values as an open symbol that are connected with dashed lines. Error bars show  $1\sigma$  uncertainties. Using the environmental mask, we label the location of each environment. The bottom right-hand panel shows a map of galactocentric radius, where we colour code each radial bin.

on the ‘effective width’ approach (Heyer, Carpenter & Snell 2001; Leroy et al. 2016, 2017a; Sun et al. 2018; Querejeta et al. 2019), in which the velocity dispersion is computed as

$$\sigma_{\text{Line}} = \frac{I_{\text{Line}}}{T_{\text{peak}} \sqrt{2\pi}}, \quad (3)$$

where  $I_{\text{Line}}$  is the line integrated intensity in  $\text{K km s}^{-1}$ , and  $T_{\text{peak}}$  is the peak brightness temperature of the spectrum in units of K. The

uncertainty of the velocity dispersion is calculated by propagating the corresponding uncertainties. The velocity dispersion is determined within lines of sight with S/N greater than 7 in both HCN and CO(2–1). We show our results in Fig. 6 where we colour code our points according to their CO(2–1) integrated intensity. We see that HCN line profiles become broader with brighter CO(2–1) emission. This is also the case for CO(2–1), which was previously highlighted by Sun et al. (2018, 2020). Here we also compare our results with velocity dispersion measures within the literature.

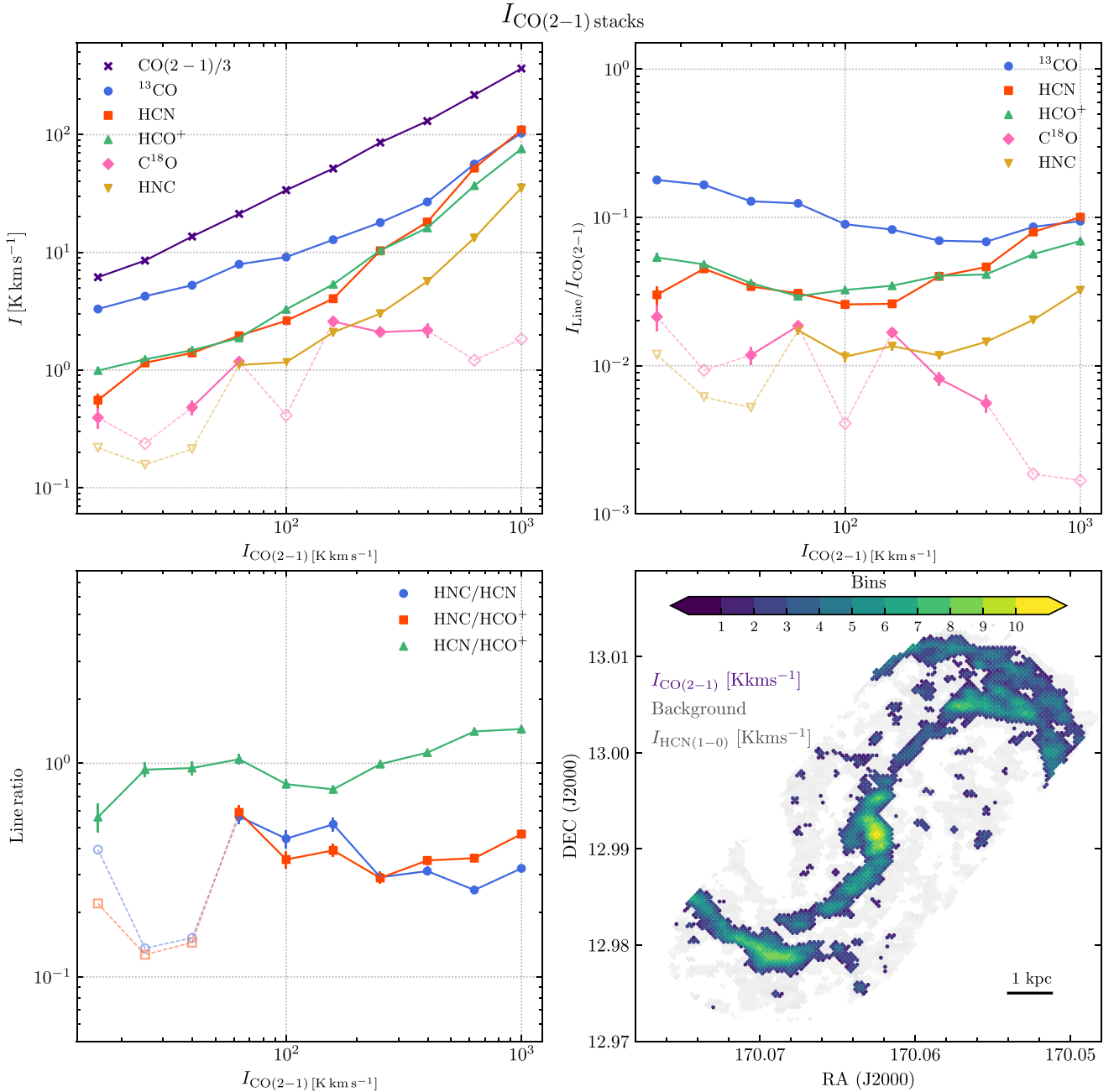


**Figure 4.** Same as Fig. 3, but stacked by CO(2–1). In this case, we only use data points with  $S/N > 12$  in CO(2–1). We show the HCN integrated intensity map in grey in the bottom right-hand panel. Coloured points represent the lines of sight that contribute to CO(2–1) bins.

Several works within the literature have also made a similar comparison to that presented in this section, albeit over various spatial scales using fundamentally different observations and methods to determine the velocity dispersion. Hence, a direct comparison is difficult and should be taken with caution. Anderson et al. (2014) investigated the velocity dispersions of dense molecular clumps at 1.45 pc resolution in the 30 Doradus region within the Large Magellanic Cloud. Their result is that HCN and  $\text{HCO}^+$  velocity dispersions of molecular clumps in 30 Doradus are comparable with CO velocity dispersions, concluding that the denser molecular gas is not dynamically decoupled from the bulk molecular gas. They also found a trend of increasing clump brightness with increasing

velocity dispersion. Jiménez-Donaire et al. (2017) measured HCN,  $\text{HCO}^+$ , and  $^{13}\text{CO}$  line widths in six galaxies, including NGC 3627, at 1 kpc resolution from a Gaussian fit of radially stacked spectra. They found narrower line widths in the discs of their galaxies than in their centres. In the case of NGC 3627, the reason for the broad line widths in the central region is that there are unresolved rotational motions in the centre, as well as the motions along the spiral arms and the bar.

Querejeta et al. (2019) investigated the velocity dispersions of dense gas tracers in M51 over spatial scales ( $\sim 100$  pc) similar to those in our work. Importantly, this study used the same approach when calculating the ‘effective’ velocity dispersion, therefore we can



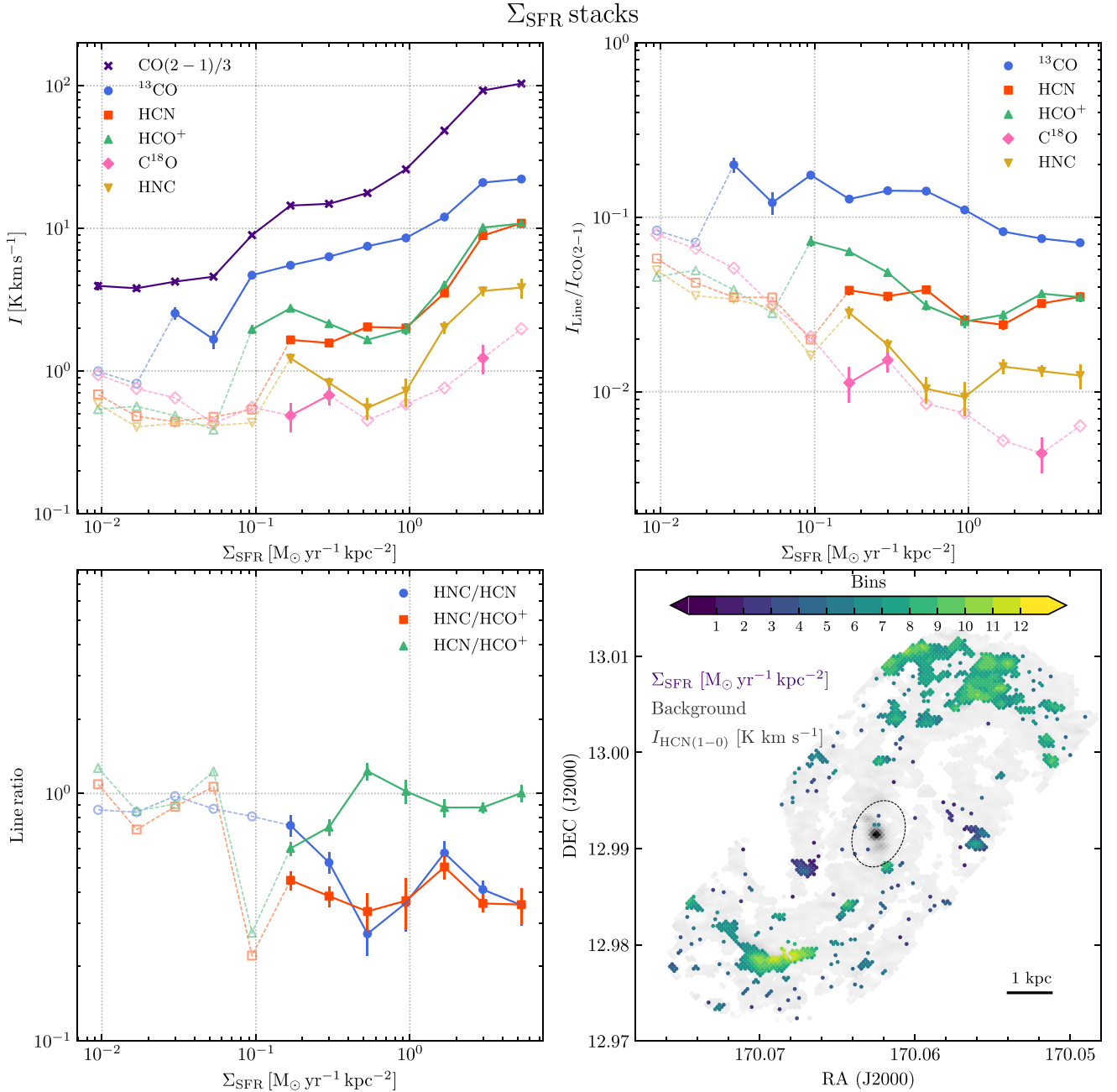


**Figure 5.** Same as Fig. 3, but for stacks by  $\Sigma_{\text{SFR}}$ . We stack data points from regions where star formation is traced by  $\text{H}\alpha$  emission (Section 2.3). We exclude the centre (region within the circle with radius of  $\sim 600$  pc) where  $\text{H}\alpha$  emission may not exclusively trace recent star formation. We also show the HCN integrated intensity map in grey in the bottom right-hand panel.

directly compare our results with Querejeta et al. (2019). We show points from Querejeta et al. (2019) as grey circles in Fig. 6. The velocity dispersions seen for sightlines coming from NGC 3627 are higher than those seen in M51 in both HCN and CO(2–1). There seems to be a consistent picture, where broader profiles of HCN correlate with broader and brighter CO profiles, which is then suggestive that we probe multiple clouds along the line of sight. Thus our results are also in agreement with Querejeta et al. (2019) and the studies mentioned in the paragraph above.

In Fig. 6, we see that there is a deviation from the 1 : 1 relation as the HCN velocity dispersion is lower than the velocity dispersion

of CO(2–1) emission. This behaviour likely arises due to the HCN emission being less spatially extended than the CO(2–1) (see Section 3.1 and Fig. 2), which is expected also to be seen in velocity space, or due to the presence of more gas traced by CO(2–1). Larger velocity dispersion can result from the presence of complex line profiles. We see only a few sightlines where velocity dispersions are higher in HCN than in CO(2–1) and these come from the sightlines with the brightest CO(2–1) emission in NGC 3627.

To compare velocity dispersion across different regions in NGC 3627, we label points coming from the centre of NGC 3627 as stars with a red outline, whereas the sightlines coming from the

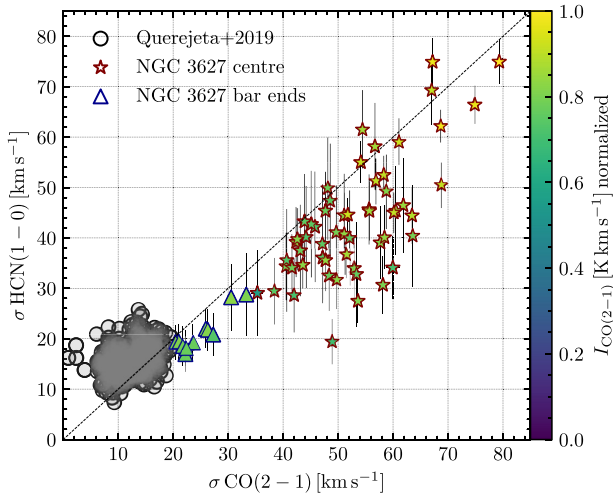


**Figure 6.** HCN velocity dispersion in comparison with CO(2–1) velocity dispersion. We show velocity dispersion measurements from Querejeta et al. (2019) as grey circles, whereas coloured points are sightlines from NGC 3627 colour coded according to their CO(2–1) integrated intensity. The dashed line shows where the points would lie in case of equal velocity dispersion in HCN and CO(2–1) emission. The points from the centre of NGC 3627 are marked as stars with a red outline, whereas points coming from the bar ends are labelled as blue triangles.

bar ends are marked as triangles with a blue outline in Fig. 6. Here we indeed see that velocity dispersions in the centre are higher than those from the bar ends. The deviation seen in the HCN–CO(2–1) velocity dispersion in the centre continues further from the centre.

There could be several explanations for these systematic differences in the HCN line profiles relative to the CO emission. Towards the centre and bright star-forming regions infrared pumping of HCN could also broaden the velocity dispersion relative to CO (Matsushita et al. 2015). Another explanation is that HCN and CO(2–1) may populate different orbits. CO(2–1) line profile exhibits multiple velocity components across some sightlines that can broaden the line. For complex line profiles, it is possible that HCN is not tracing all the velocity components in CO(2–1). The main difference in velocity dispersion seen in the centre and the bar ends is that in the very centre HCN and CO(2–1) trace the same molecular gas, i.e. the mean gas density in the centre might be higher than the HCN and CO(2–1) effective critical densities (Table 2). In the bar ends, however, the mean gas density is lower than the HCN effective critical density, therefore, HCN and CO(2–1) do not trace the same gas. In conclusion, the HCN velocity dispersion relative to CO(2–1) can be an identifier for complex line profiles. The importance of investigating each velocity component was demonstrated in Henshaw et al. (2020). We expand this analysis later, where we link the presence of complex line profiles in CO(2–1) with HCN emission in bar ends (Section 4.4).

### 3.5 Line ratios

In this section, we present the results for different velocity-integrated brightness temperature line ratios (hereafter line ratios). Investigating the line ratios, we are able to access the physics and chemistry that describes molecular gas better than investigating line intensities themselves. We derived these line ratios from the spectral stacking procedure, for bins of CO(2–1) integrated intensity,  $\Sigma_{\text{SFR}}$ , and

galactocentric radius (see Section 3.2). The error on the line ratio is calculated by the propagation of the uncertainties for the respective integrated line intensities,

$$\Delta_{\text{Line1}/\text{Line2}} = \left| \frac{I_{\text{Line1}}}{I_{\text{Line2}}} \right| \sqrt{\left( \frac{\Delta_{\text{Line1}}}{I_{\text{Line1}}} \right)^2 + \left( \frac{\Delta_{\text{Line2}}}{I_{\text{Line2}}} \right)^2}, \quad (4)$$

where  $I_{\text{Line}i}$  is a given integrated line intensity and  $\Delta_{\text{Line}i}$  is its uncertainty within each bin (their computation is described in Section 3.2), both in units of  $\text{K km s}^{-1}$ . The computed line ratio and the associated uncertainty are non-dimensional.

In the following, we focus in more detail on the ratios of lines relatively to CO(2–1) and the ratios between denser gas tracers (HNC/HCN, HCN/HCO<sup>+</sup>, and HNC/HCO<sup>+</sup>).

#### 3.5.1 Line ratios with respect to CO(2–1) integrated intensity

We examine how the line intensities over the CO(2–1) integrated intensity vary as a function of morphology across NGC 3627, CO(2–1) emission, where the CO(2–1) is assumed to trace the cloud-scale molecular surface density,  $\Sigma_{\text{mol}}$ . We also look at how the ratio of the line intensities over the CO(2–1) varies as a function of SFR surface density,  $\Sigma_{\text{SFR}}$ . These line ratios are shown in the top right-hand panels in Figs 3–5.

First, we discuss the line ratios of the CO isotopologues. In Fig. 3, we show line intensities over the CO(2–1) integrated intensity as a function of the galactocentric radius. We find that the  $^{13}\text{CO}/\text{CO}(2-1)$  line ratio has the highest values across NGC 3627, with average values of  $0.129 \pm 0.005$ . We see that  $^{13}\text{CO}/\text{CO}(2-1)$  is lower in the centre and inner bar than compared to the outer bar region and the bar ends. The variation of  $^{13}\text{CO}/\text{CO}(2-1)$  is 0.6 dex across a radial range of  $\sim 5$  kpc.

In the top right-hand panel of Fig. 4, we show the line ratios as a function of CO(2–1) integrated intensity. The  $^{13}\text{CO}/\text{CO}(2-1)$  ratio appears to slightly decrease with increasing CO(2–1) integrated intensity. The average  $^{13}\text{CO}/\text{CO}(2-1)$  ratio over the CO(2–1) bins is  $0.109 \pm 0.002$ . We find that  $^{13}\text{CO}/\text{CO}(2-1)$  varies over 0.4 dex, whereas the CO(2–1) integrated intensity varies by 2 dex.

Similarly, we find in the top right-hand panel of the Fig. 5 that the  $^{13}\text{CO}(1-0)/\text{CO}(2-1)$  ratio decreases with increasing  $\Sigma_{\text{SFR}}$ . The average  $^{13}\text{CO}/\text{CO}(2-1)$  line ratio is  $0.126 \pm 0.006$  and this line ratio varies over 0.4 dex whilst  $\Sigma_{\text{SFR}}$  varies over  $\sim 3$  orders of magnitude.

The  $\text{C}^{18}\text{O}/\text{CO}(2-1)$  line ratio has the lowest values compared to the remaining line ratios we show here and also the lowest number of significant points. We find a value for  $\text{C}^{18}\text{O}/\text{CO}(2-1)$  of  $(12 \pm 2) \times 10^{-3}$  in the bar end of NGC 3627, and in the spiral arms it is  $(14 \pm 3) \times 10^{-3}$  (top right-hand panel in Fig. 3). As a function of CO(2–1) and  $\Sigma_{\text{SFR}}$ , the mean  $\text{C}^{18}\text{O}/\text{CO}(2-1)$  ratio is  $0.014 \pm 0.002$ .

We now discuss the ratios of the remaining line integrated intensities over CO(2–1) emission. These line ratios are used as a proxy of the dense gas fraction (e.g. HCN/CO). The HCN/CO(2–1) integrated intensity can also be used to describe the dense gas fraction,  $f_{\text{dense}}$ , since the CO(2–1)/CO(1–0) is well studied (Sandstrom et al. 2013; Law et al. 2018; den Brok et al. 2021).

As a function of the environment (the top right-hand panel of Fig. 3), HCN/CO(2–1) line ratio has the highest measured value of  $0.071 \pm 0.001$  in the centre of NGC 3627, after which slightly decreases towards the bar. The average line ratio across NGC 3627 is  $0.046 \pm 0.003$ . HCN/CO(2–1) in the central region is  $\sim 2$  times higher than in the bar ends. From the top right-hand panel in Fig. 4, we report mean HCN/CO(2–1) line ratio of  $0.046 \pm 0.001$ . The

biggest value of  $0.100 \pm 0.004$ , in this case, is found in the very centre of NGC 3627.

In case of CO(2–1) bins (top right-hand panel in Fig. 4), it appears that HCN/CO(2–1) has two regimes where the intersecting point is at the CO(2–1) integrated intensity of  $100 \text{ K km s}^{-1}$ . We find HCN/CO(2–1) is almost constant in the first regime where the CO(2–1) integrated intensity changes by an order of magnitude. In the second regime, we find that the HCN/CO(2–1) ratio varies by over 0.6 dex. In the top right-hand panel in Fig. 5, HCN/CO(2–1) ratio has significant points from  $\Sigma_{\text{SFR}}$  values of  $10^{-1} \text{ M}_{\odot} \text{ yr}^{-1} \text{ kpc}^{-2}$ . Here HCN/CO(2–1) varies over 0.2 dex and the average line ratio is  $0.035 \pm 0.002$ . The maximum value of  $0.038 \pm 0.002$  is found in the lowest recoverable  $\Sigma_{\text{SFR}}$  bin, while in the very last  $\Sigma_{\text{SFR}}$  we report a slightly lower value of this line ratio.

The rest of the line ratios (HCO<sup>+</sup>/CO(2–1) and HNC/CO(2–1)) show a similar behaviour as the HCN/CO(2–1). HCO<sup>+</sup>/CO(2–1) and HNC/CO(2–1) have average values of  $0.047 \pm 0.003$  and  $0.018 \pm 0.002$ , respectively, across NGC 3627. We find higher values of HCN/CO(2–1) in the centre of NGC 3627 than the HCO<sup>+</sup>/CO(2–1), whereas it becomes vice versa in the bar ends. At the high-intensity end HCN/CO(2–1) becomes overluminous compared to HCO<sup>+</sup>/CO(2–1) (top right-hand panel in Figs 3 and 4). As a function of CO(2–1) emission (top right-hand panel in Fig. 4), both the HCO<sup>+</sup>/CO(2–1) and the HNC/CO(2–1) vary over 0.4 dex. The average line ratios are  $0.044 \pm 0.001$  for the HCO<sup>+</sup>/CO(2–1) and  $0.017 \pm 0.001$  for the HNC/CO(2–1). We report similar variation of these two line ratios as a function of  $\Sigma_{\text{SFR}}$  (Fig. 5), where HCO<sup>+</sup>/CO(2–1) and HNC/CO(2–1) vary by  $\sim 0.5$  dex. The average line ratios in this case are  $0.042 \pm 0.002$  for HCO<sup>+</sup>/CO(2–1) and  $0.015 \pm 0.002$  for HNC/CO(2–1).

Here we list our results and compare them with previous studies of NGC 3627 at lower spatial resolution. We find a peak HCN/CO(2–1) ratio of 0.076 in the very centre of NGC 3627, and a mean value of  $0.058 \pm 0.002$  across the central 1 kpc (see Fig. 3). Similarly, across the central 1 kpc of NGC 3627, the studies of Gallagher et al. (2018b) and Jiménez-Donaire et al. (2019), who conduct a comparable stacking analysis, report mean a HCN/CO(1–0) ratio of  $\sim 0.04$ . The HCO<sup>+</sup>/CO(2–1) in the centre of NGC 3627 is 0.078, and  $0.047 \pm 0.002$  the mean value in the inner 1 kpc region. For the HCO<sup>+</sup>/CO(1–0) line ratio, Jiménez-Donaire et al. (2019) found a value of 0.017 at 1 kpc from the centre, whilst Gallagher et al. (2018a) reported a value of 0.039 in the centre and 0.01 at 1 kpc from the centre. Overall, our values towards the centre agree well with previous studies at lower spatial resolution, if we take into account the mean CO(2–1)/CO(1–0) ratio of 0.59 in NGC 3627 (den Brok et al. 2021). Comparing ratios determined here to the literature at larger Galactic radii is not possible, as our mosaic is not fully complete for bins  $> 2$  kpc (see lower right-hand panel of Fig. 3).

### 3.5.2 Line ratios of HCN, HNC, and HCO<sup>+</sup>

In this section, we investigate the line ratios between the tracers of denser molecular gas, i.e. HNC/HCN, HCO<sup>+</sup>/HCN, and HNC/HCO<sup>+</sup>, as a function of three different stacking properties (bottom left-hand panels of Figs 3–5).

The HNC/HCN ratio is considerably lower than unity as a function of all the stacking properties. When considering only the significant points for the HNC/HCN ratio as a function of galactocentric radius (the bottom left-hand panel in Fig. 3), the average HNC/HCN line ratio across NGC 3627 is  $0.30 \pm 0.03$ . The mean value of HNC/HCN ratio in the inner 1.2 kpc region is  $0.30 \pm 0.05$  that is in agreement with the

one reported by Jiménez-Donaire et al. (2019) for the inner 1.2 kpc region of five barred galaxies ( $0.4 \pm 0.1$ ). Watanabe et al. (2019) found a value of  $0.3 \pm 0.1$ . HNC/HCN does not vary with the CO(2–1) emission, but we report a slightly higher value of this line ratio for CO(2–1) integrated intensities below  $200 \text{ K km s}^{-1}$ . The mean HNC/HCN line ratio within all the CO(2–1) bins is  $0.387 \pm 0.024$ , whereas it is  $0.46 \pm 0.06$  as a function of the  $\Sigma_{\text{SFR}}$ .

As a function of the environment in NGC 3627, we find HCN/HCO<sup>+</sup> greater than unity in the central region. We measure the highest value ( $1.9 \pm 0.4$ ) in the bar around 2 kpc, whereas we report values lower than unity in the bar ends where we measure the minimum value of this line ratio ( $0.42 \pm 0.08$ ). At the very centre of NGC 3627 we find HCN/HCO<sup>+</sup> to be  $1.27 \pm 0.02$ . Overall, we find the mean HCN/HCO<sup>+</sup> to be  $(1.31 \pm 0.06)$  in the inner 1.2 kpc region, and both Jiménez-Donaire et al. (2019) and Watanabe et al. (2019) reported  $1.3 \pm 0.2$ . For the CO(2–1) stacks (the bottom left-hand panel in Fig. 4), we find values lower than unity at CO(2–1) integrated intensities below  $200 \text{ K km s}^{-1}$ , whereas regions with brighter CO(2–1) emission have HCN/HCO<sup>+</sup> values above unity. The variation of HCN/HCO<sup>+</sup> is 0.5 dex across two orders of magnitude in CO(2–1). From the bottom left-hand panel in Fig. 5, we find an average HCN/HCO<sup>+</sup> ratio of  $0.91 \pm 0.08$ . Here HCN/HCO<sup>+</sup> varies over 0.3 dex.

The HNC/HCO<sup>+</sup> ratio has a value below unity in all three cases. The mean HNC/HCO<sup>+</sup> ratio across NGC 3627 is  $0.32 \pm 0.04$ . The HNC/HCO<sup>+</sup> ratio varies over 0.3 dex as a function of CO(2–1) and over 0.2 dex as a function of  $\Sigma_{\text{SFR}}$ .

## 4 DISCUSSION

In this work, we observe high critical density molecules (HCN, HNC, and HCO<sup>+</sup>) and CO isotopologues (<sup>13</sup>CO and C<sup>18</sup>O) across the disc of the star-forming galaxy NGC 3627 at scales of 100 pc comparable to individual GMCs. We use CO(2–1) data from PHANGS-ALMA as a bulk molecular gas tracer (Leroy et al. 2021b) and extinction-corrected H $\alpha$  emission from PHANGS-MUSE as a star formation tracer (Emsellem et al., in preparation).

The observed molecular lines show emission about 10–100 times fainter than the CO(2–1) line. We directly detect HCN and HCO<sup>+</sup> emission in the brightest regions of NGC 3627 – the centre and bar ends. To recover the faint emission from the observed lines and increase the S/N, we make use of the stacking technique described in Section 3.2. Data are stacked by three different parameters that are measured at high resolution: galactocentric radius, CO(2–1) integrated intensity, and  $\Sigma_{\text{SFR}}$ . Our key results are presented in Section 3.

### 4.1 Integrated intensities

From the top left-hand panel of Fig. 3, we note that there is a lack of emission along the inner part of the bar (1.2–2.2 kpc), except for the brightest observed line in our sample, <sup>13</sup>CO. We investigate line intensity profiles across different environments where we were able to recover emission over significantly extended continuous areas (the brightest regions in NGC 3627: the inner 1.2 kpc region and the bar ends). In this section, we discuss how the line ratios vary within these two environments, as well as how the environment sets the star formation and denser gas fraction, and mention some caveats of our work.

Overall, we recover significant emission for all of our lines in bins of CO(2–1) intensity and  $\Sigma_{\text{SFR}}$ . We find that all lines show a positive correlation with CO(2–1) emission. They follow the structure of the



CO(2–1) emission, and show the brightest emission in the centre and the bar ends, as well where  $\Sigma_{\text{SFR}}$  is enhanced. Since CO(2–1) emission traces the molecular cloud scale surface density, our result is expected from the assumption that the denser molecular gas is found in regions where more gas is present.

#### 4.2 Dense gas fraction across different environments: the centre and the bar end

Ratios involving HCN/CO(2–1), HNC/CO(2–1), and HCO<sup>+</sup>/CO(2–1) can indicate how the gas is distributed across a range of densities, as these tracers have a high contrast of critical density (see Table 2 and Shirley 2015).

The HCN/CO line ratio, which is thought to be a good indicator of the dense gas fraction  $f_{\text{dense}}$ , appears to be bigger in regions of galaxies with high stellar mass surface density, high gas surface density, and high dynamical pressure (Usero et al. 2015; Bigiel et al. 2016; Jiménez-Donaire et al. 2017, 2019). This trend has been found with observations at  $\sim 1$  kpc resolution, whereas at the 100 pc spaces studied here we expect to see more variations with local environment and stochasticity (due to time evolution; Schrubba et al. 2010; Querejeta et al. 2019). To first order,  $f_{\text{dense}}$  and  $\text{SFE}_{\text{dense}}$  are a function of galactocentric radius. A similar result has also been presented in recent studies at sub-kpc ( $\sim 500$  pc) scales by Gallagher et al. (2018a,b) and Querejeta et al. (2019).

Gallagher et al. (2018b) found that the HCN/CO(2–1) ratio is higher in the inner kpc of four nearby galaxies (barred galaxies NGC 3351, NGC 3627, and NGC 4321 and unbarred galaxy NGC 4254). We find that the HCN/CO(2–1) ratio is elevated in the centre of NGC 3627 by approximately a factor of 2, compared to the bar-end regions (see Fig. 3). One possible explanation for this elevated HCN/CO(2–1) ratio, and hence higher denser gas fraction, is that the bar is driving a significant amount of gas towards the centre, which leads to an accumulation of (denser) molecular gas (Sheth et al. 2005; Krumholz & Kruijssen 2015; Sormani, Binney & Magorrian 2015a,b; Tress et al. 2020). It is worth mentioning that other effects may play a role in enhancing the HCN/CO(2–1) ratio (e.g. see Barnes et al. 2020a). For example, HCN emission can be enhanced relative to CO emission due to the presence of a very strong IR emitting source (i.e. via radiative IR pumping; e.g. Matsushita et al. 2015). CO(2–1) could have a high optical depth in some regions, which would cause a relative decrease in its emission relative to HCN emission. Moreover, the centre of NGC 3627 hosts an AGN (Filho et al. 2000).

Our results indicate that the HCN/CO(2–1) ratio, interpreted to trace the dense gas fraction  $f_{\text{dense}}$ , appears not to correlate with H $\alpha$  emission on  $\sim 100$  pc scales in NGC 3627 (see Fig. 5). Gallagher et al. (2018a) showed that  $f_{\text{dense}}$  positively correlates with the star formation efficiency of molecular gas ( $\text{SFE}_{\text{mol}}$ ) even though a significant scatter is present. These authors also found that  $f_{\text{dense}}$  correlates more strongly with the dense gas star formation efficiency ( $\text{SFE}_{\text{dense}}$ ) as compared to  $\text{SFE}_{\text{mol}}$  (see figs 6 and 7 in Gallagher et al. 2018a).  $\text{SFE}_{\text{dense}}$  is a strong function of the environment, i.e. it appears to be reduced in regions of high molecular gas surface density and high stellar surface density (Shetty et al. 2014a; Shetty, Clark & Klessen 2014b). Murphy et al. (2015) found similar results for NGC 3627: they showed that  $\text{SFE}_{\text{mol}}$  anticorrelates with  $f_{\text{dense}}$  in the centre and the bar ends. This study also suggested that the dynamical state of dense gas sets this reduced star formation efficiency.

In Fig. 7, we compare the extinction-corrected H $\alpha$ /HCN luminosity ratio as a function of the HCN/CO(2–1) luminosity ratio for all positions with significant CO and HCN emission. To extract sightlines from different environments, we apply environmental

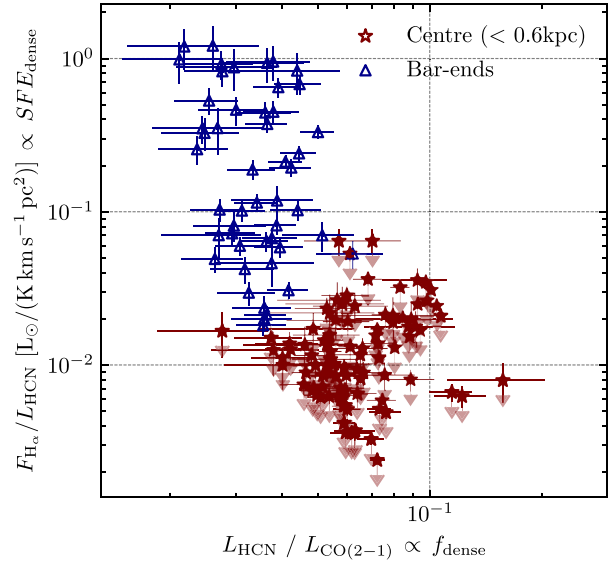


**Figure 7.** H $\alpha$ /HCN luminosity ratio versus HCN/CO(2–1) luminosity ratio that can be thought of as proxies of  $\text{SFE}_{\text{dense}}$  and  $f_{\text{dense}}$ , respectively. Shown as red and blue points are independent sightlines we extract using the environmental masks (Querejeta, in preparation). These sightlines are coming from the centre and the bar ends of NGC 3627, respectively. The central  $\text{SFE}_{\text{dense}}$  points should be considered as upper limits due to the additional contribution of H $\alpha$  emission not attributed to star formation (see Section 2.3.2).

masks to our data: we assign points coming from the centre of NGC 3627 (inner radius of 600 pc region) and points that belong to the spiral arm or the bar (bar ends). The points are colour coded according to the environment from which they come. We find that central and bar-end positions have relatively similar values of HCN/CO(2–1) with mean  $f_{\text{dense}} \sim 0.025$  and  $\sim 0.04$ , spanning less than an order of magnitude,  $f_{\text{dense}} \sim 0.015$ – $0.1$ . However, we find that they have significantly different H $\alpha$ /HCN values with mean  $\text{SFE}_{\text{dense}} \sim 0.01$  and  $\sim 0.1$  in the centre and bar end, respectively. We recapitulate (see Section 2.3) that it is, however, likely that a large fraction of the H $\alpha$  emission in the centre of NGC 3627 is not associated with star formation, rather could be attributed to AGN activity. Therefore, the H $\alpha$  emission and, hence,  $\text{SFE}_{\text{dense}}$ , for the centre points, should be treated as upper limits (as highlighted in Fig. 7). We also highlight here a possibility of the obscured star formation in the centre, not traced by H $\alpha$  emission (as discussed in Section 2.3).

The difference in these two environments may stem from the fact that the mean gas density in the centre may be much higher than the effective critical density of HCN (Leroy et al. 2017a), which increases  $f_{\text{dense}}$ . However, as previously mentioned, it has been proposed that it is the *relative* overdensities within the gas that are susceptible to gravitational collapse and form stars. That said, despite having a large  $f_{\text{dense}}$ , the galaxy centre would have a lower  $\text{SFE}_{\text{dense}}$ . Such a trend is observed within both the Milky Way’s centre (e.g. Longmore et al. 2013; Kruijssen et al. 2014; Barnes et al. 2017) and other galaxy centres (e.g. Usero et al. 2015; Bigiel et al. 2016; Jiménez-Donaire et al. 2019). Helfer & Blitz (1997) explained a high HCN/CO(1–0) ratio in the centre of NGC 5194 by the presence of the AGN. HCN/CO(2–1) ratio found in the centre of NGC 3627 could be explained by invoking suppressed star formation. We also note that at the small spatial scales ( $\sim 100$  pc) studied in this work, the scatter that

can be seen in Fig. 7 can be affected or driven by evolutionary effects in the gas–star cycle as the region separation lengths are  $\sim 100$ – $250$  pc (Kruijssen & Longmore 2014; Kruijssen et al. 2018; Chevance et al. 2020). At the centre, however, that is most likely not the case as the fragmentation length of the gas reservoir is much smaller there as shown in e.g. Henshaw, Longmore & Kruijssen (2016), unless the entire centre goes through a feeding/starburst cycle (e.g. Kruijssen et al. 2014; Sormani & Barnes 2019; Barnes et al. 2020b). Other potential mechanisms regulating and suppressing star formation in the centre could be turbulence, suggested by the observed large velocity dispersions in both CO(2–1) and HCN (see Fig. 6), the effects of magnetic fields, and the increased gravitational potential of disc and bulge, though their roles are less clear (Krumholz & Kruijssen 2015). With this discussion in mind, however, it should be mentioned that a difference in the chemistry of these regions could also result in the observed scatter. Galactic Centres are known to harbour higher cosmic ionization rates than disc regions, which can lead to the formation and distinction of molecules, and increase or decrease their respective abundances (e.g. Harada et al. 2015). This is discussed further in the following section.

### 4.3 Line ratios between HCN, HNC, and HCO<sup>+</sup>

Ratios among high critical density lines, i.e. HCN, HNC, and HCO<sup>+</sup>, may encode information about density variations, radiation field, chemistry, and optical depth. The use of these line ratios to distinguish these properties is discussed in this section.

#### 4.3.1 Does the HCN/HCO<sup>+</sup> ratio highlight X-ray-dominated regions?

The HCN/HCO<sup>+</sup> line intensity ratio is not driven by a single process, but it is more of an interplay between radiation field, column density, and gas density (Privon et al. 2015). The HCN/HCO<sup>+</sup> ratio is thought to be a good tracer of X-ray-dominated regions (XDRs; Murphy et al. 2015; Privon et al. 2015), because HCN abundance relative to CO and HCO<sup>+</sup> can be X-ray enhanced due to the presence of AGN (Jackson et al. 1993; Tacconi et al. 1994; Kohno et al. 2001; Usero et al. 2004), even though there are some sources with an AGN that do not show this. According to Meijerink, Spaans & Israel (2007), the HCN/HCO<sup>+</sup> ratio can be used to discriminate between XDR and photon-dominated region (PDR). Krips et al. (2008) found a systematic difference in HCN/HCO<sup>+</sup> between AGN and starburst-dominated systems. Moreover, Privon et al. (2015) concluded that global HCN enhancement is not necessarily a tracer of an AGN, whereas the presence of AGN does enhance HCN emission.

On the one hand, both HCN and HCO<sup>+</sup> are sensitive to cosmic rays. HCO<sup>+</sup> is produced predominantly by the CO + H<sub>3</sub><sup>+</sup> reaction, where H<sub>3</sub><sup>+</sup> is created by cosmic ray ionization of H<sub>2</sub> (Caselli et al. 1998). Therefore, we expect a higher HCO<sup>+</sup> abundance when the cosmic ray ionization rate is high. However, very high ionization rates may boost HCN emission by increasing the number of HCN–electron collisions (Kauffmann et al. 2017). On the other hand, HCO<sup>+</sup> as an ion tends to recombine and it is sensitive to the free electron abundance, although we would still expect the cosmic ray ionization rate to boost the HCO<sup>+</sup>. HCN abundance, however, is not dependent on the free electron abundance (Papadopoulos 2007). Besides abundance and electron density, this line ratio can also be affected by the optical depth as shown by Jiménez-Donaire et al. (2017). This study calculated the optical depth of HCN ( $\tau = 4.2 \pm 0.5$ ) and HCO<sup>+</sup> ( $\tau < 5.2$ ) in NGC 3627 from the

HCN/H<sup>13</sup>CN and HCO<sup>+</sup>/H<sup>13</sup>CO<sup>+</sup> line ratios. Moreover, if HCN and HCO<sup>+</sup> are optically thick (Jiménez-Donaire et al. 2017) and subthermally excited across the galaxy’s disc (Knudsen et al. 2007; Meier et al. 2015), then the HCN/HCO<sup>+</sup> ratio may remain close to unity with small changes across the disc. Within resolved Galactic star-forming regions, the above effects combine to produce a spatial offset between HCN and HCO<sup>+</sup> that highlights this line ratio as a tool to trace fundamentally different environmental conditions (e.g. Pety et al. 2017; Barnes et al. 2020a). Murphy et al. (2015) reported a spatial offset between HCN and HCO<sup>+</sup> peak emission in NGC 3627’s bar ends, implying that excitation effects may also play a role.

There is significant evidence to suggest that NGC 3627 harbours an AGN in its centre, which is classified as LINER/type 2 Seyfert galaxy (Ho et al. 1997; Filho et al. 2000; Véron-Cetty & Véron 2006). NGC 3627 hosts a strong X-ray source in its centre (Grier et al. 2011), which could affect the surrounding gas and impact the HCN/HCO<sup>+</sup> line ratio.

Our results show that the HCN/HCO<sup>+</sup> line ratio has values greater than or close to unity in the central region of NGC 3627 (see Fig. 3). HCN/HCO<sup>+</sup> ratio higher than unity is characteristic of either a high-density PDR ( $n_{\text{H}} > 10^5 \text{ cm}^{-3}$ ) or a low column density XDR ( $N_{\text{H}} < 3.16 \times 10^{22} \text{ cm}^{-2}$ ; Meijerink et al. 2007). The presence of a XDR would cause CO(2–1)/CO(1–0) ratio being well above unity. Law et al. (2018) found a CO(2–1)/CO(1–0) ratio of  $\sim 0.5$ – $0.6$  in the nuclear region of NGC 3627 combining a CO(2–1) observations from the Submillimeter Array (SMA) at 1 arcsec resolution and CO(1–0) from a BIMA Survey of Nearby Galaxies (BIMA SONG; Regan et al. 2001; Helfer et al. 2003) at 5 arcsec resolution. CO(2–1)/CO(1–0) ratio found in the centre of NGC 3627 is lower than the values found in XDR models (Meijerink et al. 2007), which is then suggestive that most of the CO(2–1) emission does not come from an XDR. Moreover, we estimate the X-ray flux from the AGN integrated over 2–10 keV (Ho et al. 1997; Filho et al. 2000). The flux is computed at a distance of approximately the beam size 100 pc from the AGN and it is  $\sim 2.6 \times 10^{-3} \text{ erg cm}^{-2} \text{ s}^{-1}$ . This value is lower than the fluxes used in the Meijerink & Spaans (2005) models, which indicates that X-ray emission gets significantly absorbed very close ( $< 100$  pc) to the AGN, and, therefore, should not impact the HCO<sup>+</sup>/HCN line ratio at larger radii.

We further consider possible composite XDR and PDR as explanations for the observed HCN/HCO<sup>+</sup> ratio. Privon et al. (2015) reported HCN/HCO<sup>+</sup> ratio of 1.84 for an AGN-dominated system, 1.14 for composite (high-density environments such as molecular cloud cores), and 0.88 for starburst systems. García-Burillo et al. (2014) found an average HCN/HCO<sup>+</sup> value of 2.5 in nuclear centre of NGC 1068 at 35 pc resolution. They reported the lowest HCN/HCO<sup>+</sup> value of 1.3. We report the average HCN/HCO<sup>+</sup> value in the centre of NGC 3627 to be  $1.31 \pm 0.06$  and the lowest HCN/HCO<sup>+</sup> value of  $1.07 \pm 0.07$  within the central region. According to Privon et al. (2015), the average HCN/HCO<sup>+</sup> in the central region of NGC 3627 is lying between the AGN-dominated and composite systems.

X-ray sources have also been found in the bar ends of NGC 3627 (Weżgowiec, Soida & Bomans 2012), where we report a mean HCN/HCO<sup>+</sup> ratio of  $\sim 0.85$ . The X-ray luminosity from the bar ends integrated over 0–3 keV ( $\sim 3.5 \times 10^{38}$  and  $4 \times 10^{38} \text{ erg s}^{-1}$  for the southern and the northern bar ends, respectively) is comparable with the X-ray luminosity integrated over the same range from the centre ( $\sim 2.75 \times 10^{38} \text{ erg s}^{-1}$ ; Weżgowiec et al. 2012). The X-ray emission in the bar ends could then also be influencing the HCO<sup>+</sup>/HCN ratio within the bar ends, but at spatial scales lower than the beam size ( $\sim 100$  pc).

#### 4.3.2 HNC/HCN ratio as a temperature tracer

Recently, Hacar, Bosman & van Dishoeck (2020) have suggested that the HNC/HCN line ratio probes the gas kinetic temperature in the molecular interstellar medium (ISM). This dependence was, however, determined using high spatial resolution ( $<0.1$  pc) observations of the Orion star-forming region. Hence, it is interesting to apply this probe to our NGC 3627 observations that cover a much larger dynamic range of environments both within the map and within the large beam ( $\sim 100$  pc). Theoretical studies have suggested that the observed variations in HCN and HNC emission could be chemically controlled. HCN can be produced in neutral–neutral collisions ( $\text{HNC} + \text{H} \rightarrow \text{HCN} + \text{H}$ ), which when proceeding from left to right lowers the HNC/HCN abundance ratio. This reaction activates at a certain temperature, although there are some discrepancies between the observations and theoretical models. Schilke et al. (1992) calculated the activation temperature of 200 K, Talbi, Ellinger & Herbst (1996) found value of a 2000 K, whereas recent studies showed that this reaction could be activated at temperatures as low as  $\sim 20$  K (Graninger et al. 2014). Gas chemistry should also be taken into account, as it can enhance HCN abundance at temperatures between 30 and 60 K, and therefore influence HNC/HCN abundance ratio (Graninger et al. 2014).

Overall, we find the HNC/HCN line ratio to be less than unity within all three different types of bins shown in Figs 3–5. We also find that there is no correlation with CO(2–1) intensity, and the HNC/HCN ratio does not vary within the star formation bins; e.g. assuming star formation could correlate with gas temperature. Moreover, we see that the HNC/HCN ratio is higher in the bar end than in the centre. If we assume the temperature dependence of HNC/HCN in our case, as derived by Hacar et al. (2020) within the Orion integral shaped filament, we estimate a mean beam-averaged temperature in the centre and bar ends to be both 34 K. It is expected that higher temperatures should originate from the galactic centre region, e.g. due to the increased energetics (e.g. shocks) and/or radiation field within the central region. However, it is worth noting that NGC 3627 could be atypical as the bar ends are also very prominent in star formation and complex dynamics (i.e. that could also cause strong shocks; see Section 4.4), and it is not clear that one would then expect a relative increase in temperature towards the centre, or not a chemical, but a physical (density) effect.

Lastly, one may expect that a change in gas temperature could also affect the HCN/HCO<sup>+</sup> ratio in the same way as the HNC/HCN ratio (Jiménez-Donaire et al. 2019), albeit to a lesser degree, i.e. due to the HCN abundance variation with temperature. Indeed, we do observe larger values of the HCN/HCO<sup>+</sup> ratio within the centre compared to the disc. Yet, as previously discussed (Section 4.3.1), it is not clear if this is due to PDR and XDR, as opposed to the gas temperature.

#### 4.4 Dynamical interaction enhancing star formation in the bar ends

We now investigate dynamical effects that can affect star formation within the bar ends of NGC 3627. Bar ends are thought to be the interface of gas populating two major sets of orbits, from either the bar or the spiral arms. The bar ends happen to be the apocentres of the orbits that are elongated parallel to the bar, as the gas flows on these orbits near the bar ends (Athanasoula 1992). At the apocentres, the gas slows down and piles up, which compresses the gas and enhances star formation. Orbital crowding and the intersection of gas on such orbits (e.g. via cloud–cloud collisions), followed by compression and collapse, are thought to enhance the SFR and the star formation

efficiency in these regions (e.g. Benjamin et al. 2005; López-Corredoira et al. 2007; Renaud et al. 2015; Sormani et al. 2020).

The role of orbital motions on star formation in the northern and southern bar-end regions of NGC 3627 has been investigated by Beuther et al. (2017) using CO(2–1) line emission as a kinematic tracer. The CO(2–1) line was observed by the Plateau de Bure Interferometer (PdBI) and IRAM 30-m (Paladino et al. 2008; Leroy et al. 2009) at 1.6 arcsec (88 pc) resolution. They found that the positions of the brightest emission (i.e. integrated intensity peaks) exhibit the broadest line profiles, almost all of which consist of multiple (sometimes even more than two) velocity components in the cold denser molecular gas. These components are interpreted as resulting from the particular arrangement of the gas populating both bar and spiral orbits.

There are also a number of sightlines with lower line widths and only one velocity component. These are in agreement with the line width–size relation (Larson 1981; Solomon et al. 1987), indicating the presence of distinct molecular clouds from only one set of orbits. Single-peaked spectra at the northern bar end mainly trace the spiral component, whereas the bar component is observed in the single-peaked spectrum towards the southern bar end (Beuther et al. 2017). They then used the evidence of multiple velocity components to argue that converging flows and the resulting gas pile-up in this scenario lead to enhanced star formation in the bar ends of NGC 3627. This may stem from the influence of the interaction with the galaxy’s companion NGC 3628 (Chemin et al. 2003) in the north, which might cause gas to be more strongly arranged by the spiral than by the bar. Law et al. (2018) reported higher CO(2–1)/CO(1–0) line ratios in the regions where the interaction is closer. The difference in magnetic field strength in bar ends may also play a role: Soida et al. (2001) found two magnetic field components in NGC 3627, with the magnetic field connected to the CO emission along the western arm.

In this work, we confirm that the northern and southern bar ends of NGC 3627 contain not only bright CO(2–1) but also HCN emission, implying that they are rich in both cold molecular and denser molecular gas. The southern bar end appears to be brighter in both lines and more extended. Something similar is seen in H $\alpha$  emission suggesting that star formation is higher in this region. This supports the idea that these regions have ample fuel for intense star formation.

Our view of the kinematics of the denser gas in relation to the lower density gas traced by CO(2–1) adds another layer to the picture proposed by Beuther et al. (2017). Fig. 8 shows a comparison between the spatial and spectral distributions of the CO(2–1), HCN, and HCO<sup>+</sup> emission at the bar ends in NGC 3627. There we also highlight the distribution of H $\alpha$  emission from MUSE observations, to serve as a probe of star formation.

The left-hand panels in the first two rows show the H $\alpha$  maps of both bar-end regions overlaid with contours of H $\alpha$ , CO(2–1), and HCN in white, blue, and red, respectively. We find that HCN peaks in a different position than H $\alpha$  in the northern bar end, whereas a spatial offset between these two peaks is still present but smaller in the southern bar end.

We take averaged spectra within regions of a single beam ( $\sim 3$  arcsec = 164 pc in radius) at several positions across both bar ends, which are presented in Fig. 8. We mark the peaks of HCN emission with red crosses and the peaks of H $\alpha$  emission as white crosses. The spectra towards these two positions in both bar ends are shown in the right-hand panels of the top two rows and in the left-hand panels of the bottom two rows in Fig. 8.

The remaining panels in the bottom two rows show three different positions taken from Beuther et al. (2017, see their fig. 3). They



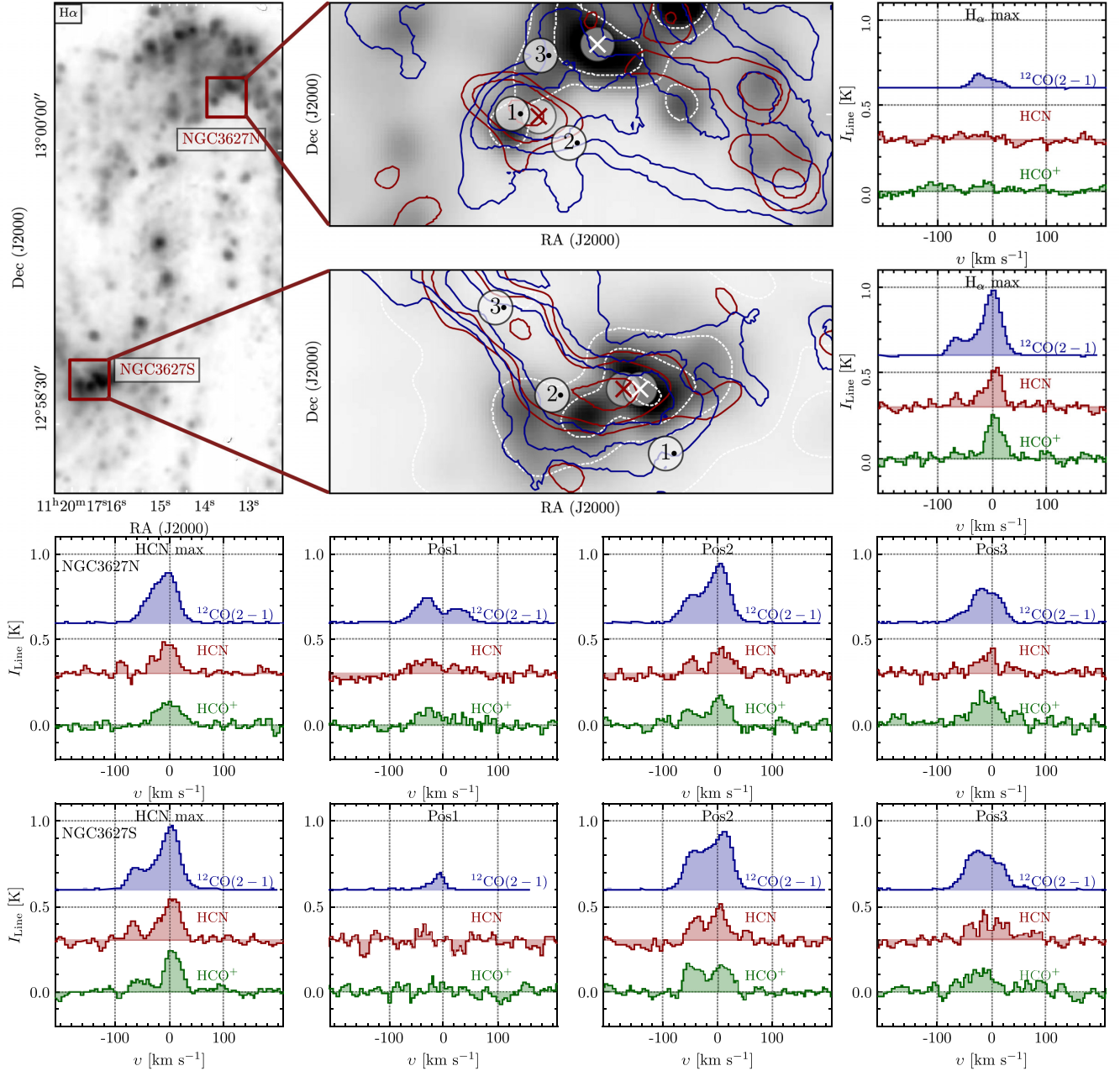


**Figure 8.** Bar-end regions within NGC 3627. The northern bar end (NGC 3627N) is shown in the top middle panel and the southern bar end (NGC 3627S) in the middle panel in the second row. We show H $\alpha$  emission within these regions in grey scale and as white contours. Contours of CO(2–1) emission (of  $50\sigma$ ,  $100\sigma$ , and  $200\sigma$ ) are shown in blue, and the HCN contours of  $3\sigma$ ,  $5\sigma$ , and  $10\sigma$  are in red. We indicate the position of the maximum of the H $\alpha$  and HCN emission with a white cross and red cross, respectively. We show averaged spectra of CO(2–1), HCN, and HCO $^+$ . In the first two rows in right-hand panels we plot spectra averaged over 3 arcsec (164 pc) region centred on the white crosses. The last two rows show averaged spectra over 3 arcsec (164 pc) region centred on the red crosses (left-hand panels), while the remaining panels show averaged spectra over 3 arcsec regions in three positions marked with numbers 1, 2, and 3 from both bar ends (each row, respectively, for NGC 3627N and NGC 3627S). These positions coincide with those analysed in Beuther et al. (2017).

identified one, two, and three CO(2–1) velocity components in the Pos1, Pos2, and Pos3 spectra, respectively. We see two or more velocity components in CO(2–1) within almost all regions shown. We also find that both the HCN and HCO $^+$  lines have two velocity components within several sightlines at the same velocities as CO(2–1).

We find that there are multiple velocity components in both HCN and HCO $^+$  emission, which appear to peak at a similar velocity and have comparable line widths to the components previously identified in CO(2–1) (Beuther et al. 2017). Moreover, we find double-peaked line profiles towards the peak of the HCN integrated intensity in

both bar ends, and a double-peaked profile towards the H $\alpha$  peak in the southern bar end. This result has two important implications. The first is the confirmation of these CO(2–1) components as real physical structures, rather than optical depth effects, as it is unlikely that both HCN and HCO $^+$  are severely optically thick and suffer from self-absorption on  $\sim 100$  pc scales. The second is then that the velocity components observed in CO(2–1), a molecular gas tracer, have significant dense gas tracer emission. This then highlights that the region contains both molecular gas and dense molecular gas that are distinct in velocity (and presumably space).

We ask then the question: How did these dense molecular gas components form? The profiles shown in Fig. 8 could suggest two scenarios. First, the dense gas could be created at the orbit intersection. Indeed, the peak of the dense gas emission within the centre of the bar-end regions would certainly point to this enhancement. Second, converging gas flows into the bar-end region could already be rich with dense gas before arrival. This could be evidence by the spectrum seen at Pos1 in the southern bar, which contains both HCN and  $\text{HCO}^+$  emission, yet sits further upstream from the bars rotation, and the bright star-forming region. Answering this question is, therefore, somewhat speculative, and in reality, the scenario is likely that both some dense gas is delivered to the bar, which then is further compressed.

There is a final interesting point to note within the southern bar-end region. This is that the good correlation between  $\text{H}\alpha$  and HCN and CO emission at the leading edge of the bar end (i.e. centre right of the zoom-in panel in Fig. 8), yet the downstream material appears to be underluminous in  $\text{H}\alpha$  for a similar amount of HCN emission (i.e. upper left of zoom-in). This then may highlight that star formation is more efficient for a given amount of dense gas within the leading edge of the bar, compared to the trailing material. This then opens a question, if not just the amount of dense gas is important in fuelling star formation, but also the dynamics of the dense gas in limiting and/or driving its collapse? In particular, if the compressing motions of the leading bar edge are enhancing star formation, whilst the shearing forces of the trailing bar end are inhibiting star formation.

#### 4.5 Systematic environmental density variations

Leroy et al. (2017a) investigated how the line intensity ratios of molecules trace molecular gas density. In extragalactic observations, reaching the necessary resolution and sensitivity while observing molecular lines fainter than CO is challenging. The line intensity integrated within a single beam encompasses a lot of different physical gas and contains information from a range of densities. The reason is that the line emits most at the ‘effective critical density’ ( $n_{\text{eff, crit}}$ ) as described in Leroy et al. (2017a), but it also emits from densities below  $n_{\text{eff, crit}}$  that frequently dominate the (subbeam) density distribution. Therefore, line intensity ratios can be used to infer density variations. We also note that optical depth, temperature, IR pumping, cosmic rays, and element abundance variations can affect the line ratios. Leroy et al. (2017a) coupled simple radiative transfer models and parametrized density probability density functions (PDFs) to quantify how changes in the subbeam density distributions affect the beam-averaged line emissivity. This study implemented two commonly considered density distributions to describe the density distribution of the cold phase of the ISM where our observed lines are produced: a pure lognormal distribution and a lognormal distribution with a power-law tail at high densities (Federrath & Klessen 2013; Girichidis et al. 2014; Kainulainen, Federrath & Henning 2014; Lombardi et al. 2014; Schneider et al. 2015a,b, 2016). They found that the subbeam density distribution affects the beam-averaged emissivity. This result is interpreted in a way that lines that trace denser gas (i.e. lines with high effective critical density) are the most sensitive to density changes. Therefore, ratios of these line’s intensities to CO lead to more variation than lines that trace pure molecular or bulk molecular gas ( $^{13}\text{CO}$ , CO(2–1)). Such a line ratio shows a different behaviour that depends on the density distribution for a fixed abundance. The shape of the distribution of molecular gas also sets the variation of line ratios. For example, HCN/CO shows greater scatter when molecular gas is described with the lognormal distribution as opposed to the case when

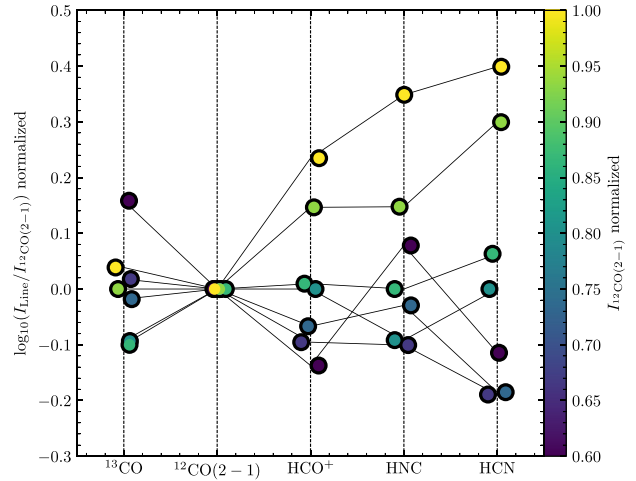


**Figure 9.** Line-to-CO(2–1) integrated intensity ratios. Individual data points are from stacking spectra by CO(2–1). We only show points at which all stacked intensities have signal/noise greater than 7 (see solid points in the top right-hand panel of Fig. 4). All points for each line ratio (same x-axis label) are normalized by their respective median value. Points are colour coded according to CO(2–1) integrated intensity (normalized) and are slightly offset along the x-axis for visualization purposes. All points with the same normalized CO(2–1) value are connected with a black line.

the lognormal distribution with a power-law tail describes molecular gas.

In this section, we investigate the scenario from Leroy et al. (2017a) that line intensity ratios can reflect changes in density distributions. In Fig. 9, we show how the line intensity ratios vary as a function of the CO(2–1) integrated intensity, used as a proxy for the volume density at cloud scales (Leroy et al. 2016; Sun et al. 2018). All intensities are determined by stacking in bins of CO(2–1) integrated intensity and only keeping significant measurements. We colour code each stacked line ratio measurement by the (normalized) CO(2–1) integrated intensity. Points with the same colour (similar ‘density bin’) are connected with a black line (see caption for details). We sort the line-to-CO(2–1) ratios according to their effective critical density listed in Table 2.

We show points at which the CO(2–1) integrated intensity is above  $\sim 50 \text{ K km s}^{-1}$ , because for these CO(2–1) intensity values the stacked line integrated intensities (except for  $\text{C}^{18}\text{O}$ ) are classified as significant (the signal/noise is  $> 7$ ) according to our criteria explained in Section 2.3 (also see Fig. 4).

Overall, we find that HCN/CO(2–1) shows the highest scatter, followed by HNC/CO(2–1) and  $\text{HCO}^+$ /CO(2–1). The flaring pattern seen in Fig. 9 is consistent with the sensitivity of these line ratios to changes in mean gas density (here as traced by cloud-scale surface density). The higher the contrast of line critical densities, the more pronounced the flaring and dynamical range. This agrees with the modelling results found in Leroy et al. (2017a) and Puschig et al. (in preparation). We note that the  $^{13}\text{CO}$ /CO(2–1) ratio shows a reversed pattern, reflecting the lower  $^{13}\text{CO}$  critical density compared to CO(2–1).

## 5 SUMMARY

We present new NOEMA observations towards a nearby, actively star-forming disc galaxy NGC 3627. These represent the current highest resolution ( $1.8 \text{ arcsec} \approx 100 \text{ pc}$ ) of molecular lines that

trace denser gas across a nearby spiral galaxy. Through this work, we investigate how the denser gas, using the following tracers HCN(1–0), HNC(1–0),  $\text{HCO}^+(1-0)$ ,  $^{13}\text{CO}(1-0)$ , and  $\text{C}^{18}\text{O}(1-0)$ , is spatially distributed across NGC 3627 in comparison with the spatial distribution of bulk molecular gas ( $\text{CO}(2-1)$  emission) and star formation ( $\text{H}\alpha$  emission). We also investigate line profiles of denser molecular gas towards the bar ends. We list our key results here.

(i) We first investigate how the observed line intensities vary as a function of the  $\text{CO}(2-1)$  emission and, therefore, as a function of the bulk molecular gas. We find that all lines show brighter emission towards regions of brighter CO emission. To inspect the second-order deviations, we investigate the ratio of the lines with respect to CO. We find that the HCN, HNC, and  $\text{HCO}^+$  to  $\text{CO}(2-1)$  ratios positively correlate with  $\text{CO}(2-1)$  emission, while the remaining lines ( $^{13}\text{CO}$  and  $\text{C}^{18}\text{O}$ ) show the opposite trend and do not correlate with  $\text{CO}(2-1)$  emission. Moreover, we test if these line ratios can trace different density distributions and investigate the scatter in the ratio with increasing CO intensity. We find that HCN, HNC, and  $\text{HCO}^+$  to  $\text{CO}(2-1)$  line ratios show greater scatter, which suggests that they trace densities above the mean molecular gas density, but it can also be driven by the other effects.

(ii) We investigate how the line intensities vary as a function of  $\text{H}\alpha$  emission. We find that all line intensities increase towards brighter  $\text{H}\alpha$  emission. Furthermore, we see that the line ratios to  $\text{CO}(2-1)$  do not vary significantly with  $\text{H}\alpha$  emission. Therefore, the line ratios show no correlation with recent star formation.

(iii) We detect significant emission in HCN,  $\text{HCO}^+$ , HNC,  $^{13}\text{CO}$ , and  $\text{C}^{18}\text{O}$  towards the brightest regions in NGC 3627 – the centre and the bar ends. Therefore, we check for trends with morphological features that describe the galaxy. The structure of the galaxy is influencing line intensities. We find that all lines show the brightest emission towards the centre and bar ends within NGC 3627. The line ratios reflect the environment: line to  $\text{CO}(2-1)$  ratios appear to be slightly higher in the centre than in the bar ends. This is a direct cause of what has been described in the former two points, i.e. looking at line intensities as a function of  $\text{CO}(2-1)$  and  $\text{H}\alpha$ . Stacking by these properties involves multiple different environments within the bins and therefore affects the trends we have seen.

(iv) We measure the velocity dispersion of HCN and  $\text{CO}(2-1)$  line emission for sightlines towards the centre and bar ends. Overall, HCN and  $\text{CO}(2-1)$  velocity dispersion increase with  $\text{CO}(2-1)$  line brightness, spanning ranges from 15 to 75  $\text{km s}^{-1}$  (20–80  $\text{km s}^{-1}$  in HCN ( $\text{CO}(2-1)$ )), while  $\text{CO}(2-1)$  changes by a factor of 1.4. The HCN velocity dispersion is lower by a few  $\text{km s}^{-1}$  than the velocity dispersion measured in  $\text{CO}(2-1)$ . Sightlines towards the centre and bar ends are located in a different part of Fig. 6. Sightlines towards the bar end exhibit considerably lower HCN (from 15 to 30  $\text{km s}^{-1}$ ) and  $\text{CO}(2-1)$  velocity dispersions (from 20 to 35  $\text{km s}^{-1}$ ) than the sightlines from the centre (from ~60 to 80  $\text{km s}^{-1}$  in both HCN and  $\text{CO}(2-1)$ ), despite having similar  $\text{CO}(2-1)$  intensity (~700 and 1000  $\text{K km s}^{-1}$  towards bar ends and centre, respectively). The difference between measured HCN and  $\text{CO}(2-1)$  velocity dispersions in the centre and bar ends could be explained due to several effects, such as IR pumping of HCN in the centre, HCN and  $\text{CO}(2-1)$  populating different orbits, and the difference in the gas mean densities from the centre and bar ends.

(v) We have probed the role of the environment on setting the star formation and thus checked the variation of the star formation efficiency with respect to the dense gas fraction on ~100 pc scales across two different environments (the centre and the bar ends). We see that they have different properties, e.g. the fraction of the

denser gas to the bulk molecular gas does not change in the bar end as much as in the centre. The  $\text{H}\alpha/\text{HCN}$  ratio, however, depends on the environment and it appears to be higher in the bar ends than in the centre. These results agree well with previous studies of  $f_{\text{dense}}$  and  $\text{SFE}_{\text{dense}}$  at coarser resolutions (Usero et al. 2015; Bigiel et al. 2016; Jiménez-Donaire et al. 2019). One possible explanation is that HCN does not trace the same amount of the denser gas in these environments, i.e. it belongs to different parts of the density distributions that describe molecular gas within these regions (lognormal and power-law tail in the centre and in the bar end, respectively). Another interpretation of this result is that gas dynamics set the star formation on these scales and therefore set the star formation efficiency of the denser gas. Since we only use extinction-corrected  $\text{H}\alpha$  emission as the star formation tracer, our results might be biased in the centre of NGC 3627.

(vi) The dynamical effects in the bar ends of NGC 3627 can enhance collisions that trigger local star formation. To investigate this, we compare the spectra of  $\text{CO}(2-1)$ , HCN, and  $\text{HCO}^+$  towards the northern and the southern bar end. We find that HCN and  $\text{HCO}^+$  have multiple velocity components associated with the  $\text{CO}(2-1)$  velocity components indicating that these gas motions coming from the spiral and the bar seen in  $\text{CO}(2-1)$  (Beuther et al. 2017) contain the denser gas. Furthermore, we note that denser gas can get piled up in the bar ends where it interacts and enhance the star formation.

Our work demonstrates the importance of pushing the observations towards high angular resolution and sensitivity to resolve and detect dense gas tracers on the scales of individual GMCs. In the future, we plan to further investigate the dynamics of the dense molecular gas, in order to understand the observed differences between environments in galaxies, such as the centre and the bar ends. It will be important to extend this work to even higher sensitivity observations, allowing us to begin to observe even fainter molecular lines in nearby galaxies (the high-J transitions of the dense molecular gas and even fainter tracers of dense molecular gas, i.e.  $\text{N}_2\text{H}^+$ ). Doing so would further our understanding of the densest ISM phase(s), and its ability to form stars.

## ACKNOWLEDGEMENTS

This work is based on IRAM/NOEMA observations carried out under project number W17BP, and the EMPIRE large program number 206-14 with the IRAM 30-m telescope. IRAM is supported by INSU/CNRS (France), MPG (Germany), and IGN (Spain). IB, ATB, FB, JPU, and JSdB would like to acknowledge the funding provided from the European Union’s Horizon 2020 Framework Programme (grant agreement no. 726384/Empire). CE acknowledges funding from the Deutsche Forschungsgemeinschaft (DFG) Sachbeihilfe, grant number BI1546/3-1. JPe and CHC acknowledge support by the Programme National ‘Physique et Chimie du Milieu Interstellaire’ (PCMI) of CNRS/INSU with INC/INP, cofunded by CEA and CNES. The work of AKL is partially supported by the National Science Foundation under grants no. 1615105, 1615109, and 1653300. AU acknowledges support from the Spanish funding grants PGC2018-094671-B-I00 (MCIU/AEI/FEDER) and PID2019-108765GB-I00 (MICINN). ES, DL, IP, TS, and FS acknowledge funding from the European Research Council (ERC) under the European Union’s Horizon 2020 Framework Programme (grant agreement no. 694343). AH was supported by the Programme National Cosmology et Galaxies (PNCG) of CNRS/INSU with INP and IN2P3, cofunded by CEA and CNES, and by the Programme National ‘Physique et Chimie du Milieu Interstellaire’ (PCMI) of CNRS/INSU with



INC/INP cofunded by CEA and CNES. CF is supported by the National Science Foundation under Award No. 1903946 and acknowledges funding from the European Research Council (ERC) under the European Union's Horizon 2020 Framework Programme (grant agreement no. 694343). KK gratefully acknowledges funding from the German Research Foundation (DFG) in the form of an Emmy Noether Research Group (grant number KR4598/2-1, PI: Kreckel). MC and JMDK gratefully acknowledge funding from the Deutsche Forschungsgemeinschaft (DFG, German Research Foundation) through an Emmy Noether Research Group (grant number KR4801/1-1) and the DFG Sachbeihilfe (grant number KR4801/2-1), and from the European Research Council (ERC) under the European Union's Horizon 2020 Framework Programme via the ERC Starting Grant MUSTANG (grant agreement number 714907). SCOG, RSK, and MCS acknowledge support from the Deutsche Forschungsgemeinschaft (DFG) via the Collaborative Research Center (SFB 881, Project-ID 138713538) 'The Milky Way System' (subprojects A1, B1, B2, and B8) and from the Heidelberg cluster of excellence (EXC 2181 - 390900948) 'STRUCTURES: A unifying approach to emergent phenomena in the physical world, mathematics, and complex data', funded by the German Excellence Strategy. RSK also thanks for funding from the European Research Council in the ERC Synergy Grant 'ECOGAL – Understanding our Galactic ecosystem: From the disk of the Milky Way to the formation sites of stars and planets' (project ID 855130). ER acknowledges the support of the Natural Sciences and Engineering Research Council of Canada (NSERC), funding reference number RGPIN-2017-03987. MCS acknowledges financial support from the German Research Foundation (DFG) via the Collaborative Research Centre (SFB 881, Project-ID 138713538) 'The Milky Way System' (subprojects A1, B1, B2, and B8). MQ acknowledges support from the research project PID2019-106027GA-C44 from the Spanish Ministerio de Ciencia e Innovación. TGW acknowledges funding from the European Research Council (ERC) under the European Union's Horizon 2020 Framework Programme (grant agreement no. 694343).

This paper makes use of the following ALMA data: ADS/JAO.ALMA#2015.1.00956.S. ALMA is a partnership of ESO (representing its member states), NSF (USA), and NINS (Japan), together with NRC (Canada), MOST and ASIAA (Taiwan), and KASI (Republic of Korea), in cooperation with the Republic of Chile. The Joint ALMA Observatory is operated by ESO, AUI/NRAO, and NAOJ. The National Radio Astronomy Observatory is a facility of the National Science Foundation operated under cooperative agreement by Associated Universities, Inc.

## DATA AVAILABILITY

The data used in this paper will be shared on reasonable request to the corresponding author.

## REFERENCES

- Anand G. S. et al., 2021, *MNRAS*, 501, 3621  
 Anderson C. N. et al., 2014, *ApJ*, 793, 37  
 André P., Di Francesco J., Ward-Thompson D., Inutsuka S.-I., Pudritz R. E., Pineda J. E., 2014, in Beuther H., Klessen R. S., Dullemond C. P., Henning T., eds, *Protostars and Planets VI*. Univ. Arizona Press, Tucson, AZ, p. 27  
 Athanassoula E., 1992, *MNRAS*, 259, 345  
 Baldwin J. A., Phillips M. M., Terlevich R., 1981, *PASP*, 93, 5  
 Barnes P. J., Muller E., Indermühle B., O'Dougherty S. N., Lowe V., Cunningham M., Hernandez A. K., Fuller G. A., 2015, *ApJ*, 812, 6  
 Barnes A. T., Longmore S. N., Battersby C., Bally J., Kruijssen J. M. D., Henshaw J. D., Walker D. L., 2017, *MNRAS*, 469, 2263  
 Barnes A. T. et al., 2020a, *MNRAS*, 497, 172  
 Barnes A. T., Longmore S. N., Dale J. E., Krumholz M. R., Kruijssen J. M. D., Bigiel F., 2020b, *MNRAS*, 498, 4906  
 Benjamin R. A. et al., 2005, *ApJ*, 630, L149  
 Beuther H., Meidt S., Schinnerer E., Paladino R., Leroy A., 2017, *A&A*, 597, A85  
 Bigiel F. et al., 2016, *ApJ*, 822, L26  
 Bolatto A. D., Wolfire M., Leroy A. K., 2013, *ARA&A*, 51, 207  
 Brouillet N., Muller S., Herpin F., Braine J., Jacq T., 2005, *A&A*, 429, 153  
 Buchbender C. et al., 2013, *A&A*, 549, A17  
 Burton M. G. et al., 2013, *Publ. Astron. Soc. Aust.*, 30, e044  
 Caldu-Primo A., Schruba A., 2016, *AJ*, 151, 34  
 Calzetti D., Armus L., Bohlin R. C., Kinney A. L., Koornneef J., Storchi-Bergmann T., 2000, *ApJ*, 533, 682  
 Calzetti D. et al., 2007, *ApJ*, 666, 870  
 Casasola V., Hunt L. K., Combes F., García-Burillo S., Neri R., 2011, *A&A*, 527, A92  
 Caselli P., Walmsley C. M., Terzieva R., Herbst E., 1998, *ApJ*, 499, 234  
 Chemin L., Cayatte V., Balkowski C., Marcelin M., Amram P., van Driel W., Flores H., 2003, *A&A*, 405, 89  
 Chen H., Braine J., Gao Y., Koda J., Gu Q., 2017, *ApJ*, 836, 101  
 Chevance M. et al., 2020, *MNRAS*, 493, 2872  
 Colombo D. et al., 2014, *ApJ*, 784, 3  
 Cormier D. et al., 2018, *MNRAS*, 475, 3909  
 Dame T. M., Hartmann D., Thaddeus P., 2001, *ApJ*, 547, 792  
 den Brok J. S. et al., 2021, *MNRAS*, 504, 3221  
 Domínguez A. et al., 2013, *ApJ*, 763, 145  
 Egusa F., Hirota A., Baba J., Muraoka K., 2018, *ApJ*, 854, 90  
 Engargiola G., Plambeck R. L., Rosolowsky E., Blitz L., 2003, *ApJS*, 149, 343  
 Evans N. J., II, Heiderman A., Vutisalchavakul N., 2014, *ApJ*, 782, 114  
 Faesi C. M., Lada C. J., Forbrich J., 2018, *ApJ*, 857, 19  
 Federrath C., Klessen R. S., 2012, *ApJ*, 761, 156  
 Federrath C., Klessen R. S., 2013, *ApJ*, 763, 51  
 Filho M. E., Barthel P. D., Ho L. C., 2000, *ApJS*, 129, 93  
 Gallagher M. J. et al., 2018a, *ApJ*, 858, 90  
 Gallagher M. J. et al., 2018b, *ApJ*, 868, L38  
 Gao Y., Solomon P. M., 2004a, *ApJS*, 152, 63  
 Gao Y., Solomon P. M., 2004b, *ApJ*, 606, 271  
 Gao Y., Carilli C. L., Solomon P. M., Vanden Bout P. A., 2007, *ApJ*, 660, L93  
 García A. M., 1993, *A&AS*, 100, 47  
 García-Burillo S. et al., 2003, in Collin S., Combes F., Shlosman I., eds, *ASP Conf. Ser. Vol. 290, Active Galactic Nuclei: From Central Engine to Host Galaxy*. Astron. Soc. Pac., San Francisco, p. 423  
 García-Burillo S., Usero A., Alonso-Herrero A., Graciá-Carpio J., Pereira-Santaella M., Colina L., Planesas P., Arribas S., 2012, *A&A*, 539, A8  
 García-Burillo S. et al., 2014, *A&A*, 567, A125  
 Girichidis P., Konstantin L., Whitworth A. P., Klessen R. S., 2014, *ApJ*, 781, 91  
 Graciá-Carpio J., García-Burillo S., Planesas P., 2008, *Ap&SS*, 313, 331  
 Graninger D. M., Herbst E., Öberg K. I., Vasyunin A. I., 2014, *ApJ*, 787, 74  
 Gratier P. et al., 2012, *A&A*, 542, A108  
 Grier C. J., Mathur S., Ghosh H., Ferrarese L., 2011, *ApJ*, 731, 60  
 Hacar A., Bosman A. D., van Dishoeck E. F., 2020, *A&A*, 635, A4  
 Harada N. et al., 2015, *A&A*, 584, A102  
 Heiderman A., Evans N. J., II, Allen L. E., Huard T., Heyer M., 2010, *ApJ*, 723, 1019  
 Helfer T. T., Blitz L., 1997, *ApJ*, 478, 162  
 Helfer T. T., Thornley M. D., Regan M. W., Wong T., Sheth K., Vogel S. N., Blitz L., Bock D. C. J., 2003, *ApJS*, 145, 259  
 Henshaw J. D., Longmore S. N., Kruijssen J. M. D., 2016, *MNRAS*, 463, L122  
 Henshaw J. D. et al., 2020, *Nat. Astron.*, 4, 1064  
 Herrera C. N. et al., 2020, *A&A*, 634, A121  
 Heyer M., Dame T. M., 2015, *ARA&A*, 53, 583  
 Heyer M. H., Carpenter J. M., Snell R. L., 2001, *ApJ*, 551, 852

- Hirota A., Kuno N., Sato N., Nakanishi H., Tosaki T., Sorai K., 2011, *ApJ*, 737, 40
- Ho L. C., Filippenko A. V., Sargent W. L. W., 1997, *ApJS*, 112, 315
- Hughes A. et al., 2013, *ApJ*, 779, 46
- Jackson J. M., Paglione T. A. D., Ishizuki S., Nguyen-Q-Rieu, 1993, *ApJ*, 418, L13
- Jiang X.-J. et al., 2020, *MNRAS*, 494, 1276
- Jiménez-Donaire M. J. et al., 2017, *MNRAS*, 466, 49
- Jiménez-Donaire M. J., 2019, *ApJ*, 880, 127
- Jones P. A. et al., 2012, *MNRAS*, 419, 2961
- Juneau S., Narayanan D. T., Moustakas J., Shirley Y. L., Bussmann R. S., Kennicutt R. C. J., Vanden Bout P. A., 2009, *ApJ*, 707, 1217
- Kainulainen J., Federrath C., Henning T., 2014, *Science*, 344, 183
- Kauffmann G. et al., 2003, *MNRAS*, 346, 1055
- Kauffmann J., Goldsmith P. F., Melnick G., Tolls V., Guzman A., Menten K. M., 2017, *A&A*, 605, L5
- Kennicutt R. C., Evans N. J., 2012, *ARA&A*, 50, 531
- Kennicutt R. C., Jr et al., 2009, *ApJ*, 703, 1672
- Kepley A. A., Leroy A. K., Frayer D., Usero A., Marvil J., Walter F., 2014, *ApJ*, 780, L13
- Kepley A. A. et al., 2018, *ApJ*, 862, 120
- Kewley L. J., Dopita M. A., Sutherland R. S., Heisler C. A., Trevena J., 2001, *ApJ*, 556, 121
- Kim J. et al., 2021, *MNRAS*, 504, 487
- Knudsen K. K., Walter F., Weiss A., Bolatto A., Riechers D. A., Menten K., 2007, *ApJ*, 666, 156
- Kohno K., Matsushita S., Vila-Vilaró B., Okumura S. K., Shibatsuka T., Okiura M., Ishizuki S., Kawabe R., 2001, in Knapen J. H., Beckman J. E., Shlosman I., Mahoney T. J., eds, ASP Conf. Ser. Vol. 249, The Central Kiloparsec of Starbursts and AGN: The La Palma Connection. Astron. Soc. Pac., San Francisco, p. 672
- Kreckel K. et al., 2019, *ApJ*, 887, 80
- Krips M., Neri R., García-Burillo S., Martín S., Combes F., Graciá-Carpio J., Eckart A., 2008, *ApJ*, 677, 262
- Kroupa P., 2001, *MNRAS*, 322, 231
- Kruijssen J. M. D., Longmore S. N., 2014, *MNRAS*, 439, 3239
- Kruijssen J. M. D., Longmore S. N., Elmegreen B. G., Murray N., Bally J., Testi L., Kennicutt R. C., 2014, *MNRAS*, 440, 3370
- Kruijssen J. M. D., Schruha A., Hygate A. P. S., Hu C.-Y., Haydon D. T., Longmore S. N., 2018, *MNRAS*, 479, 1866
- Kruijssen J. M. D. et al., 2019, *Nature*, 569, 519
- Krumholz M. R., Kruijssen J. M. D., 2015, *MNRAS*, 453, 739
- Lada C. J., Lada E. A., 2003, *ARA&A*, 41, 57
- Lada C. J., Lombardi M., Alves J. F., 2010, *ApJ*, 724, 687
- Lada C. J., Forbrich J., Lombardi M., Alves J. F., 2012, *ApJ*, 745, 190
- Larson R. B., 1981, *MNRAS*, 194, 809
- Law C. J., Zhang Q., Ricci L., Petipas G., Jiménez-Donaire M. J., Ueda J., Lu X., Dunham M. M., 2018, *ApJ*, 865, 17
- Lee J. C. et al., 2009, *ApJ*, 706, 599
- Lee J. C. et al., 2021, preprint ([arXiv:2101.02855](https://arxiv.org/abs/2101.02855))
- Leroy A. K. et al., 2009, *AJ*, 137, 4670
- Leroy A. K. et al., 2016, *ApJ*, 831, 16
- Leroy A. K. et al., 2017a, *ApJ*, 835, 217
- Leroy A. K. et al., 2017b, *ApJ*, 846, 71
- Leroy A. K. et al., 2019, *ApJS*, 244, 24
- Leroy A. K. et al., 2021a, *ApJS*, in press ([arXiv:2104.07665](https://arxiv.org/abs/2104.07665))
- Leroy A. K. et al., 2021b, *ApJS*, in press ([arXiv:2104.07739](https://arxiv.org/abs/2104.07739))
- Lombardi M., Bouy H., Alves J., Lada C. J., 2014, *A&A*, 566, A45
- Longmore S. N. et al., 2013, *MNRAS*, 429, 987
- López-Corredoira M., Cabrera-Lavers A., Mahoney T. J., Hammersley P. L., Garzón F., González-Fernández C., 2007, *AJ*, 133, 154
- Maeda F., Ohta K., Fujimoto Y., Habe A., 2020, *MNRAS*, 493, 5045
- Matsushita S., Trung D.-V., Boone F., Krips M., Lim J., Muller S., 2015, *ApJ*, 799, 26
- Meidt S. E. et al., 2018, *ApJ*, 854, 100
- Meier D. S. et al., 2015, *ApJ*, 801, 63
- Meijerink R., Spaans M., 2005, *A&A*, 436, 397
- Meijerink R., Spaans M., Israel F. P., 2007, *A&A*, 461, 793
- Mizuno A., Fukui Y., 2004, in Clemens D., Shah R., Brainerd T., eds, ASP Conf. Ser. Vol. 317, Milky Way Surveys: The Structure and Evolution of our Galaxy. Astron. Soc. Pac., San Francisco, p. 59
- Moriguchi Y., Yamaguchi N., Onishi T., Mizuno A., Fukui Y., 2001, *PASJ*, 53, 1025
- Murphy E. J. et al., 2011, *ApJ*, 737, 67
- Murphy E. J. et al., 2015, *ApJ*, 813, 118
- Osterbrock D. E., 1989, *Ann. New York Acad. Sci.*, 571, 99
- Osterbrock D. E., 1993, *ApJ*, 404, 551
- Paladino R., Murgia M., Tarchi A., Moscadelli L., Comito C., 2008, *A&A*, 485, 679
- Papadopoulos P. P., 2007, *ApJ*, 656, 792
- Pety J., 2005, in Casoli F., Contini T., Hameury J. M., Pagani L., eds, SF2A-2005: Semaine de l'Astrophysique Française. EDP Sciences, Les Ulis, France, p. 721
- Pety J., Rodríguez-Fernández N., 2010, *A&A*, 517, A12
- Pety J. et al., 2013, *ApJ*, 779, 43
- Pety J. et al., 2017, *A&A*, 599, A98
- Privon G. C. et al., 2015, *ApJ*, 814, 39
- Querejeta M. et al., 2019, *A&A*, 625, A19
- Regan M. W., Thornley M. D., Helfer T. T., Sheth K., Wong T., Vogel S. N., Blitz L., Bock D. C. J., 2001, *ApJ*, 561, 218
- Renaud F. et al., 2015, *MNRAS*, 454, 3299
- Rodríguez-Fernández N., Pety J., Gueth F., 2008, Single-Dish Observation and Processing to Produce the Short-Spacing Information for a Millimeter Interferometer. Technical Report, IRAM Memo 2008-2
- Rosolowsky E., 2007, *ApJ*, 654, 240
- Rosolowsky E., Leroy A., 2006, *PASP*, 118, 590
- Rosolowsky E., Engargiola G., Plambeck R., Blitz L., 2003, *ApJ*, 599, 258
- Rosolowsky E. et al., 2021, *MNRAS*, 502, 1218
- Sandstrom K. M. et al., 2013, *ApJ*, 777, 5
- Schilke P., Walmsley C. M., Pineau Des Forets G., Roueff E., Flower D. R., Guilloteau S., 1992, *A&A*, 256, 595
- Schinnerer E. et al., 2013, *ApJ*, 779, 42
- Schinnerer E. et al., 2019, *ApJ*, 887, 49
- Schneider N. et al., 2015a, *A&A*, 575, A79
- Schneider N. et al., 2015b, *A&A*, 578, A29
- Schneider N. et al., 2016, *A&A*, 587, A74
- Schöier F. L., van der Tak F. F. S., van Dishoeck E. F., Black J. H., 2005, *A&A*, 432, 369
- Schruba A., Leroy A. K., Walter F., Sandstrom K., Rosolowsky E., 2010, *ApJ*, 722, 1699
- Schruba A. et al., 2011, *AJ*, 142, 37
- Schruba A. et al., 2017, *ApJ*, 835, 278
- Sheth K., Vogel S. N., Regan M. W., Thornley M. D., Teuben P. J., 2005, *ApJ*, 632, 217
- Sheth K., Vogel S. N., Wilson C. D., Dame T. M., 2008, *ApJ*, 675, 330
- Shetty R., Kelly B. C., Rahman N., Bigiel F., Bolatto A. D., Clark P. C., Klessen R. S., Konstantin L. K., 2014a, *MNRAS*, 437, L61
- Shetty R., Clark P. C., Klessen R. S., 2014b, *MNRAS*, 442, 2208
- Shirley Y. L., 2015, *PASP*, 127, 299
- Soida M., Urbanik M., Beck R., Wielebinski R., Balkowski C., 2001, *A&A*, 378, 40
- Solomon P. M., Rivolo A. R., Barrett J., Yahil A., 1987, *ApJ*, 319, 730
- Sormani M. C., Barnes A. T., 2019, *MNRAS*, 484, 1213
- Sormani M. C., Binney J., Magorrian J., 2015a, *MNRAS*, 449, 2421
- Sormani M. C., Binney J., Magorrian J., 2015b, *MNRAS*, 451, 3437
- Sormani M. C., Tress R. G., Glover S. C. O., Klessen R. S., Battersby C. D., Clark P. C., Hatchfield H. P., Smith R. J., 2020, *MNRAS*, 497, 5024
- Stetson P. B., 1987, *PASP*, 99, 191
- Sun J. et al., 2018, *ApJ*, 860, 172
- Sun J. et al., 2020, *ApJ*, 901, L8
- Tacconi L. J., Genzel R., Blietz M., Cameron M., Harris A. I., Madden S., 1994, *ApJ*, 426, L77
- Talbi D., Ellinger Y., Herbst E., 1996, *A&A*, 314, 688
- Thilker D. A., Braun R., Walterbos R. A. M., 2000, *AJ*, 120, 3070
- Thuan T. X., Izotov Y. I., 2005, *ApJS*, 161, 240

- Tress R. G., Sormani M. C., Glover S. C. O., Klessen R. S., Battersby C. D., Clark P. C., Hatchfield H. P., Smith R. J., 2020, *MNRAS*, 499, 4455
- Usero A., García-Burillo S., Fuente A., Martín-Pintado J., Rodríguez-Fernández N. J., 2004, *A&A*, 419, 897
- Usero A. et al., 2015, *AJ*, 150, 115
- van der Tak F. F. S., Black J. H., Schöier F. L., Jansen D. J., van Dishoeck E. F., 2007, *A&A*, 468, 627
- Véron-Cetty M. P., Véron P., 2006, *A&A*, 455, 773
- Viaene S., Forbrich J., Fritz J., 2018, *MNRAS*, 475, 5550
- Viti S. et al., 2014, *A&A*, 570, A28
- Walter F. et al., 2017, *ApJ*, 835, 265
- Watanabe Y., Nishimura Y., Sorai K., Sakai N., Kuno N., Yamamoto S., 2019, *ApJS*, 242, 26
- Weżgowiec M., Soida M., Bomans D. J., 2012, *A&A*, 544, A113
- Wu J., Evans N. J., II, Gao Y., Solomon P. M., Shirley Y. L., Vanden Bout P. A., 2005, *ApJ*, 635, L173
- Wu J., Evans N. J., II, Shirley Y. L., Knez C., 2010, *ApJS*, 188, 313
- Yamaguchi R., Saito H., Mizuno N., Mine Y., Mizuno A., Ogawa H., Fukui Y., 1999, *PASJ*, 51, 791

## APPENDIX A: ADDITIONAL FIGURES



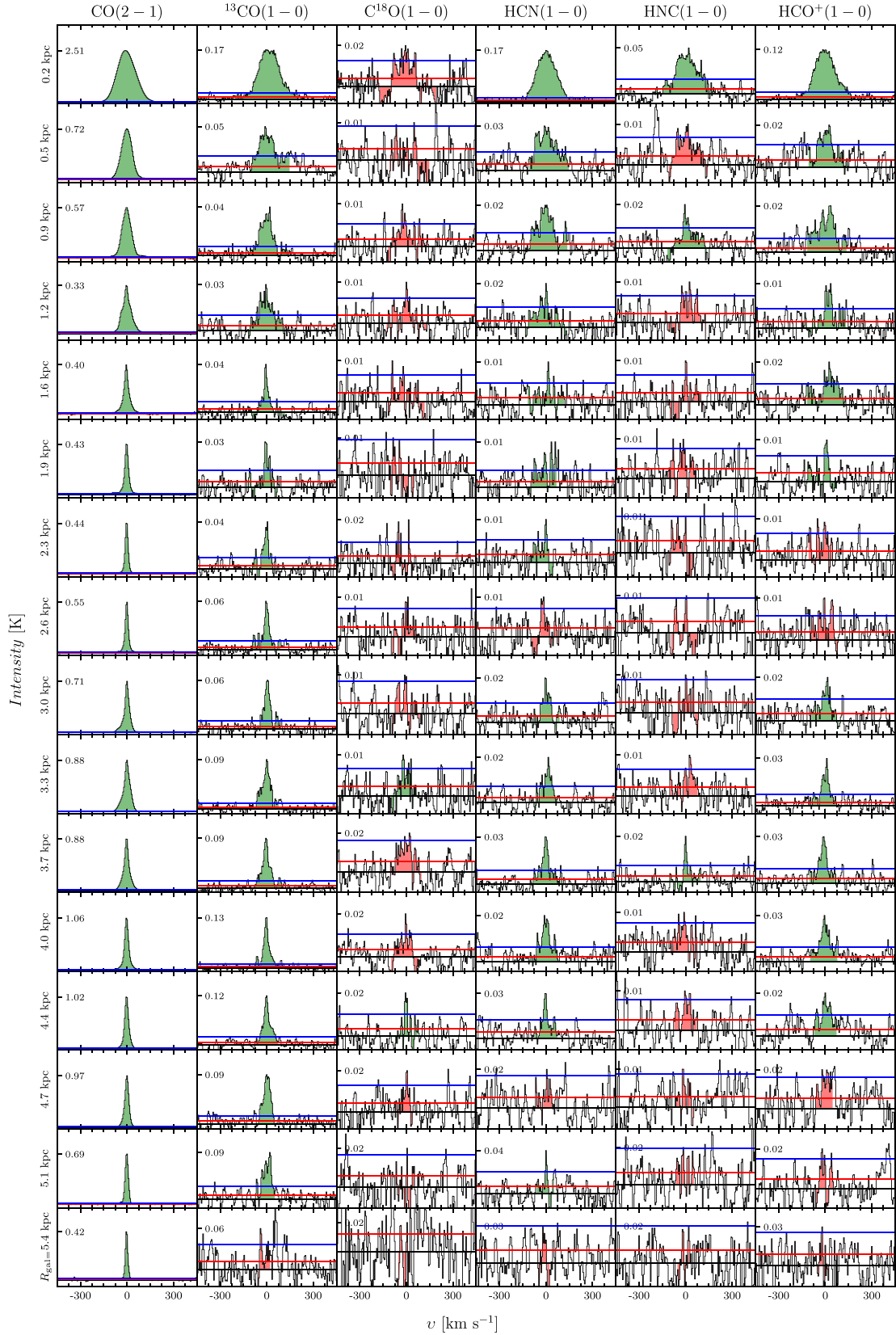


**Figure A1.** Radially stacked spectra of all lines (each column respectively). Median values of the radius for each bin are shown on the left-hand side of every row. Shaded regions show the integration window defined using CO(2–1) line. The colour of shaded regions corresponds to whether the integrated intensity of the stacked line is defined as an upper limit (red) or not (green), as described in Section 3.2. The black horizontal line shows the 0-level. The red horizontal line shows the rms of the stacked profile, whereas the blue line represents three times the rms.

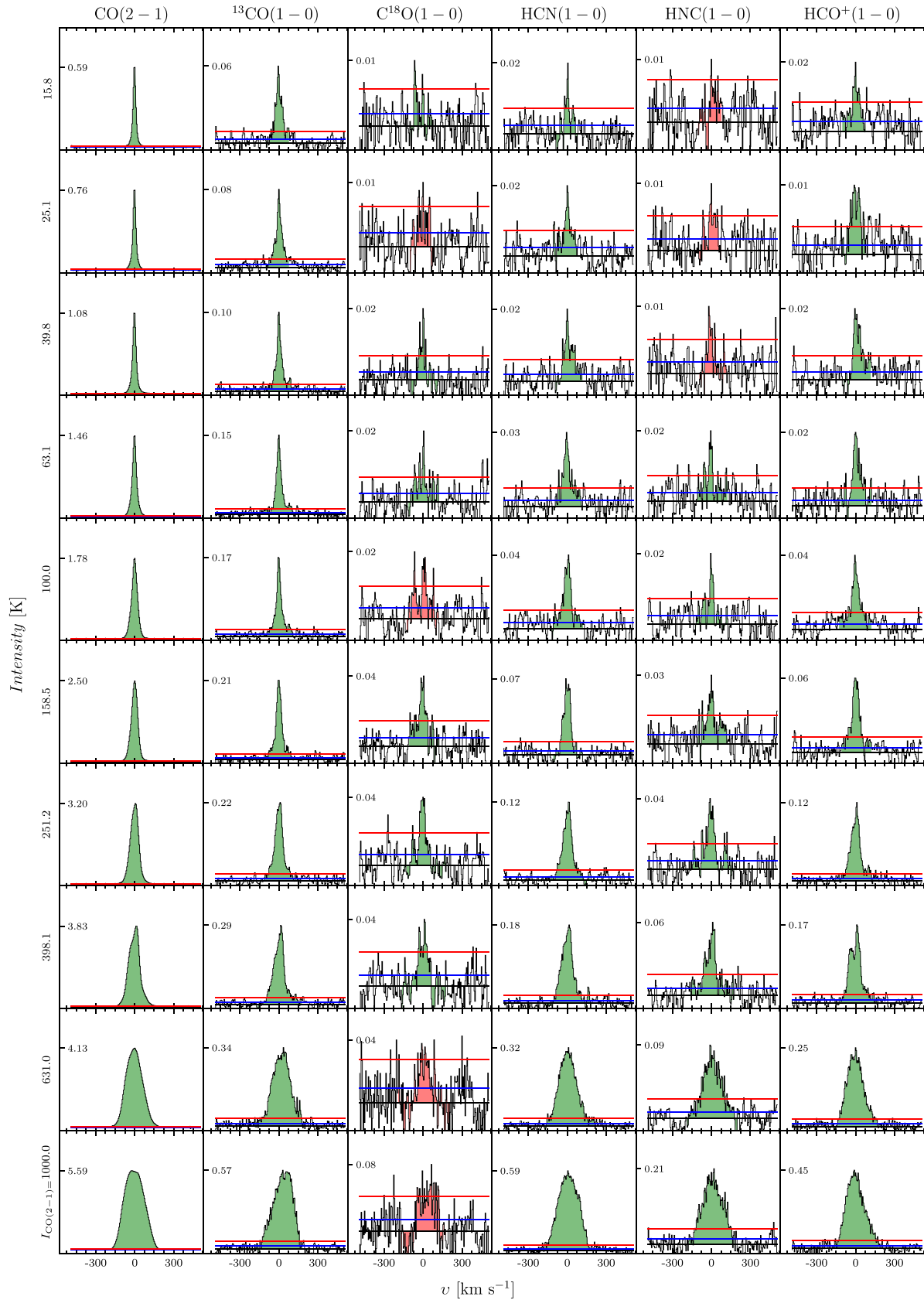


**Figure A2.** Same as in the Fig. A1, but for stacked spectra by the CO(2-1) integrated intensity. The CO(2-1) bins are in units of K km s<sup>-1</sup>.

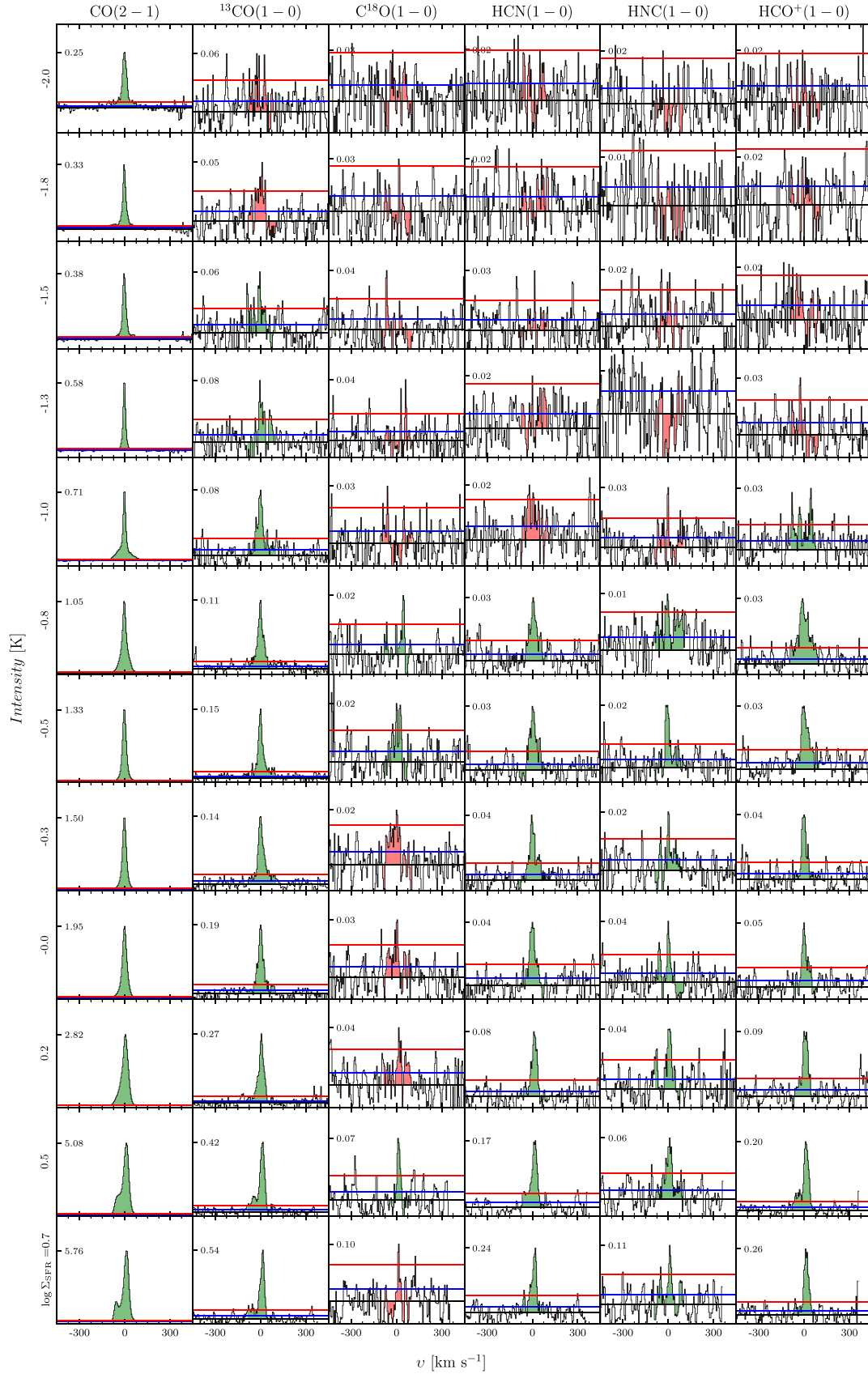


**Figure A3.** Same as in the Fig. A1, but for stacked spectra by the  $\Sigma_{\text{SFR}}$ . We show the  $\Sigma_{\text{SFR}}$  bins in logarithmic scale in units of  $\text{M}_{\odot} \text{yr}^{-1} \text{kpc}^{-2}$ .



<sup>1</sup>Argelander-Institut für Astronomie, Universität Bonn, Auf dem Hügel 71, D-53121 Bonn, Germany

<sup>2</sup>IRAM, 300 rue de la Piscine, F-38406 Saint Martin d'Hères, France

<sup>3</sup>LERMA, Observatoire de Paris, PSL Research University, CNRS, Sorbonne Universités, F-75014 Paris, France

<sup>4</sup>Department of Astronomy, The Ohio State University, 4055 McPherson Laboratory, 140 West 18th Avenue, Columbus, OH 43210, USA

<sup>5</sup>Observatorio Astronómico Nacional (IGN), C/ Alfonso XII 3, E-28014 Madrid, Spain

<sup>6</sup>Max Planck Institut für Astronomie, Königstuhl 17, D-69117 Heidelberg, Germany

<sup>7</sup>Sterrenkundig Observatorium, Universiteit Gent, Krijgslaan 281 S9, B-9000 Gent, Belgium

<sup>8</sup>European Southern Observatory, Karl-Schwarzschild Straße 2, D-85748 Garching bei München, Germany

<sup>9</sup>Univ Lyon, Univ Lyon1, ENS de Lyon, CNRS, Centre de Recherche Astrophysique de Lyon UMR5574, F-69230 Saint-Genis-Laval, France

<sup>10</sup>Université de Toulouse, UPS-OMP, F-31028 Toulouse, France

<sup>11</sup>CNRS, IRAP, Av. du Colonel Roche BP 44346, F-31028 Toulouse cedex 4, France

<sup>12</sup>Department of Astronomy, University of Massachusetts Amherst, 710 North Pleasant Street, Amherst, MA 01003, USA

<sup>13</sup>Astronomisches Rechen-Institut, Zentrum für Astronomie der Universität Heidelberg, Mönchhofstraße 12-14, D-69120 Heidelberg, Germany

<sup>14</sup>INAF – Osservatorio Astrofisico di Arcetri, Largo E. Fermi 5, I-50157 Firenze, Italy

<sup>15</sup>Institut für Theoretische Astrophysik, Zentrum für Astronomie, Universität Heidelberg, Albert-Ueberle-Straße 2, D-69120 Heidelberg, Germany

<sup>16</sup>Research School of Astronomy and Astrophysics, Australian National University, Canberra, ACT 2611, Australia

<sup>17</sup>ARC Centre of Excellence for All Sky Astrophysics in 3 Dimensions (ASTRO 3D), Mount Stromlo Rd Stromlo, Australian Capital Territory 2611, AU, Australia

<sup>18</sup>Interdisziplinäres Zentrum für Wissenschaftliches Rechnen, Universität Heidelberg, Im Neuenheimer Feld 205, D-69120 Heidelberg, Germany

<sup>19</sup>4-183 CCIS, University of Alberta, Edmonton, AB T6G 2E1, Canada

<sup>20</sup>Max Planck Institut für Extraterrestrische Physik, Giessenbachstraße 1, D-85748 Garching, Germany

This paper has been typeset from a  $\text{\LaTeX}$  file prepared by the author.